

## ABSTRACT

Title of dissertation: *Ab Initio* Lattice Dynamics  
and Infrared Dielectric Response

Hadley M. Lawler, Doctor of Philosophy, 2004

Dissertation directed by: Dr. Eric L. Shirley  
N.I.S.T.

Methods for theoretically evaluating lattice dynamics, anharmonic effects and related optical properties from first-principles are designed and implemented. Applications of density-functional theory and the pseudopotential approximation are adapted, via the Born-Oppenheimer approximation, the Hellmann-Feynman force theorem, and wave-commensurate supercells, to a direct calculation of the Born-von Karman force constants. With a symmetry analysis and interpolation of the Born-von Karman force constants, the complete phonon spectra are obtained for the cubic systems Ar, Si, Ge, and diamond, and for the stacked hexagonal system, graphite. The phonon spectra for the polar materials GaAs and GaP, in which the degeneracy between longitudinal and transverse optical modes is lifted, are also calculated. The splitting is a consequence of the macroscopic field associated with long-range Coulombic interactions and longitudinal displacements. Diagrammatically-derived expressions for the finite lifetime of the Raman mode arising from phonon-phonon interactions are calculated for Si, Ge, and diamond from first principles, and agree with experiment to within uncertainty. The infrared absorption spectra of GaAs and GaP are calculated from first principles through the phonon anharmonic self-energy (phonon-phonon interaction) and the Born effective charges (photon-phonon interaction). Several aspects of the spectra are in detailed agreement with the experimental spectra, including: the strong temperature dependence of the far-infrared absorption due to the onset of difference pro-

cesses; the linewidth and asymmetric lineshape of the reststrahlen; the spectral structure of the absorption by two-phonon modes; and overall oscillator strengths. The theory allows for the identification of narrow spectral transmission bands with an ionic mass mismatch in the case of GaP. Analytic and complete calculations are performed for the ion-ion displacement correlation function in solid Ar, and agree well. The correlations are evaluated for arbitrary lattice vector and Cartesian displacement directions, and their pressure dependence leads to the conjecture that anharmonic effects are less prominent at higher pressures.

*Ab Initio* Lattice Dynamics and  
Infrared Dielectric Response

by

Hadley M. Lawler

Dissertation submitted to the Faculty of the Graduate School of the  
University of Maryland, College Park in partial fulfillment  
of the requirements for the degree of  
Doctor of Philosophy  
2004

Advisory Committee:

Professor H. Dennis Drew, Chair/Advisor  
Dr. Eric L. Shirley, Co-Advisor  
Professor Theodore L. Einstein  
Professor Frederick C. Wellstood  
Professor Neil Goldsman

© Copyright by  
Hadley M. Lawler  
2004

## ACKNOWLEDGMENTS

My appreciation goes to: Aleksi Soininen for his assistance with the symmetry analysis; Eric Chang for the fine work he contributed; Joe Redish, whose advocacy made possible my work at Maryland; Joe and Fred Wellstood for their scientific and professional leadership; Simon Kaplan for his measurements which have strengthened this report; Jeff Simpson and Dennis Drew, for the conversations which have sharpened my understanding of phonons and optical properties; and Eric Shirley, who taught me solid-state physics and turned me toward this excellent research project. I am also grateful to my friends and family for the essential distractions, generosity, and inspiration they have offered.

## TABLE OF CONTENTS

List of Figures	v
1 Introduction	1
2 Total Energy and Ionic Forces in Crystals	3
2.1 The Adiabatic Approximation and Reduction of the Many-body Problem . . .	3
2.2 Evaluating the Electronic Ground State . . . . .	4
2.2.1 Density-Functional Theory . . . . .	4
2.2.2 The Pseudopotential Approximation . . . . .	5
2.3 The Total Energy . . . . .	6
2.4 The Hellmann-Feynman Force Theorem . . . . .	7
3 Phonon Dispersion Calculations: Si, Ge, diamond, and graphite.	8
3.1 Force Constants and the Dynamical Matrix . . . . .	8
3.2 Calculating the Dynamical Matrix . . . . .	9
3.2.1 Sampling the Brillouin Zone . . . . .	9
3.2.2 Interpolation . . . . .	12
3.3 Computational Details . . . . .	13
3.4 Uncertainties and Comparison with Experiment . . . . .	15
4 Polar Crystals: GaAs and GaP	26
4.1 Macroscopic Fields: Phonon Dispersion and Infrared Response . . . . .	26
4.2 The Modern Theory of Polarization and Calculation of the Born Effective Charges . . . . .	29
4.3 Phonon Dispersion and Macroscopic Fields . . . . .	30
4.4 Results for GaAs and GaP . . . . .	33

5	Calculation of Anharmonic Effects	39
5.1	Beyond the Harmonic Approximation . . . . .	39
5.2	Long-wave Optical Phonon Lifetime . . . . .	41
5.3	The Sublattice Displacement and Symmetry Considerations . . . . .	43
5.4	Results and Uncertainty . . . . .	44
6	Anharmonic Effects and Infrared Response	46
6.1	Phonons and Infrared Absorption . . . . .	46
6.2	Dielectric Response of the Lattice . . . . .	48
6.3	The Phonon Self-Energy . . . . .	50
6.4	Discussion . . . . .	52
7	Ionic Displacement Correlations from the Zero-point Motion of Pressurized Solid Argon	59
7.1	The Correlation Function . . . . .	59
7.2	Pressurized Solid Argon . . . . .	60
7.3	Phonon Dispersion and Elastic Constants . . . . .	61
7.4	Exact Formulas for the Correlation Function . . . . .	63
7.5	Approximate Formulas . . . . .	63
7.6	Analytical and Numerical Results at 6.7 GPa . . . . .	65
7.7	Pressure Dependence of the Correlation Function . . . . .	67
7.8	Conclusions . . . . .	67
8	Conclusions	73
A	Fitting and Interpolation Algorithm	75
	Bibliography	83

## LIST OF FIGURES

3.1	Phonon dispersion in diamond . . . . .	18
3.2	Phonon density of states in diamond . . . . .	19
3.3	Phonon dispersion in Ge . . . . .	20
3.4	Phonon density of states in Ge . . . . .	21
3.5	Phonon dispersion in Si . . . . .	22
3.6	Phonon density of states in Si . . . . .	23
3.7	Phonon dispersion in graphite . . . . .	24
3.8	Phonon density of states in graphite . . . . .	25
4.1	Phonon dispersion in GaAs . . . . .	35
4.2	Phonon density of states in GaAs . . . . .	36
4.3	Phonon dispersion in GaP . . . . .	37
4.4	Phonon density of states in GaP . . . . .	38
6.1	Infrared absorption: experiment and theory . . . . .	54
6.2	Temperature dependence of far-infrared response in GaAs . . . . .	55
6.3	Temperature dependence of far-infrared response in GaP . . . . .	56
6.4	Lowest-order processes contributing to the infrared-active phonon self-energy	56
6.5	The IR-active-phonon self-energy for GaAs at 300 K . . . . .	57
6.6	The self-energy for GaAs near the reststrahl . . . . .	57
6.7	Phonon dispersion for GaAs and GaP . . . . .	58
7.1	Calculated phonon dispersion of argon Ar at 3.1 GPa . . . . .	69
7.2	Independent correlations along the lattice-separation direction (110) in Ar at	
	6.7 GPa . . . . .	70



7.3	Independent correlations along the lattice-separation direction (200) in Ar at 6.7 GPa . . . . .	71
7.4	Scaled correlation in Ar at various pressures . . . . .	72

## Chapter 1

### Introduction

Many of the finest minds in modern physics have taken interest in the optical implications of phonon-phonon interactions in insulators. The connection between such interactions and the spectrally broad background absorption, which is observed to accompany the sharp harmonic resonances, was pointed out by Pauli [1], in a study of a linear chain. Subsequently, Born and Blackman showed that anharmonic interactions lead to secondary features in a classical theory [2]. A quantum-mechanical treatment was developed by Barnes, Brattain and Seitz [3], which emphasized secondary features but not damping, and a time-dependent perturbative formalism was developed by Born and Huang [4].

About the time Green's functions formalisms were being developed for the theory of anharmonic effects on neutron scattering from crystals [5], it was recognized that the Born-Huang theory was incomplete. The improved anharmonic dielectric formalism discussed by Maradudin and Wallis, Cowley, and Vinogradov [6] is that implemented in this work.

Although the infrared dielectric theory had been worked out, not until recently could phonon-photon and phonon-phonon interactions be calculated. The essential developments were very successful first-principles calculations of Born effective charges [7] and phonon-phonon scattering rates [8]. Prior to these theoretical developments, the realistic modeling of quantities such as a phonon lifetime was elusive, even with parameters taken from experiment [9].

The far-infrared frequency regime and the response of semiconductors are of considerable technological interest. The ability, as demonstrated in this work, to calculate from first-principles detailed frequency and temperature dependence of the dielectric response may prove to be a very useful application of modern theory.

Chapter 2 of this thesis provides an overview of the general theory and critical approximations which allow for the evaluation of ground-state energies, charge distributions, and ionic forces in crystals. Chapter 3 details the extension of these methods to the calculation of phonon dispersion and phonon spectra. Chapter 4 motivates the physics associated with macroscopic fields, in particular the relevance of macroscopic fields to dispersion and infrared dielectric response. It is seen that the Lyddane-Sachs-Teller relation expresses the close physical connection between phonon oscillator strength and the lifted degeneracy between longitudinal and transverse zero-momentum modes in polar crystals. Chapter 5 reports the formalism and details of the Raman mode lifetimes in diamond-type systems. Chapter 6 combines the theoretical approaches of Chapter 4 and Chapter 5 to present detailed infrared spectra, and temperature dependence, of GaAs and GaP. Portions of the work in Chapter 6 are to be published in Physical Review B this year.

In Chapter 7, analytic expressions for zero-temperature ionic-displacement correlations are derived, evaluated, and compared to non-analytic, numerical results. The pressure dependence of the correlations leads to the empirically untested, and perhaps counterintuitive, conjecture that the anharmonic character of a crystal is less prominent at higher pressures. Portions of this work have been published in Physical Review B **69**, 174104 (2004).

Beyond the fundamental nature of the topics discussed in this thesis, their relevance to other areas of research are discussed in Chapter 8. Refinements and extensions of the calculations reported here are also suggested.

## Chapter 2

### Total Energy and Ionic Forces in Crystals

#### 2.1 The Adiabatic Approximation and Reduction of the Many-body Problem

For the purposes of lattice dynamics, the task of simultaneously determining the states of a large number of interacting particles, both nuclei and electrons, can be conceptually and computationally simplified with invocation of the Born-Oppenheimer approximation, where for any given nuclear configuration, the electronic system is assumed to be in the ground state.

Essentially, the Born-Oppenheimer approximation replaces the full Hamiltonian of the solid, which includes kinetic energy of electrons, nuclei, and the interaction potentials,

$$H = T_{nuc} + T_{el} + U_{nuc-nuc} + U_{el-el} + U_{nuc-el}, \quad (2.1)$$

with a simplified Hamiltonian to which the nuclei are subject:

$$H_{B-O} = T_{nuc} + U_{B-O}. \quad (2.2)$$

In this form, the Hamiltonian is a function only of the nuclear coordinates and their canonical momenta. Thus the Born-Oppenheimer approximation subsumes all terms which depend on electronic coordinates and the internuclear interaction into an effective nuclear potential.

The fundamental justification for the Born-Oppenheimer approximation lies in the large ratio of nuclear to electronic masses. This implies that, with respect to time and length scales appropriate to the nuclear motion, the electrons return to equilibrium rapidly after a small nuclear displacement, so that the electronic system is capable of adiabatically following the nuclear motion.

Below, each of the terms which contribute to the Born-Oppenheimer potential—within the various further approximations to be made—are discussed.

## 2.2 Evaluating the Electronic Ground State

### 2.2.1 Density-Functional Theory

Currently realistic properties of materials are obtainable from first principles by application of the Hohenberg-Kohn theorem [10]. This theorem states that the ground-state energy can be expressed as a functional of, and can be ascertained by minimization with respect to, the electron probability density. The minimization is performed with nuclear coordinates which are assumed static, and enter the calculation classically. The functional, therefore, does not explicitly include terms which correspond to the nuclear kinetic energy and the internuclear potential in Eq. 2.1. In atomic units—where the electronic charge, the electronic mass and Bohr radius are related by  $e = m_e = a_0 = 1$ —the functional is then written:

$$E_g[n] = T_g[n] + \int d^3\mathbf{r} V_0(\mathbf{r})n(\mathbf{r}) + \frac{1}{2} \int d^3\mathbf{r}_1 \int d^3\mathbf{r}_2 \frac{n(\mathbf{r}_1)n(\mathbf{r}_2)}{|\mathbf{r}_1 - \mathbf{r}_2|} + E_{XC}[n]. \quad (2.3)$$

In this expression, the electron-electron interaction is expressed as a sum of Hartree and exchange-correlation terms, and  $V_0(\mathbf{r})$  is external to the electronic system, its source in this case being considered as the presence of nuclei. The electronic density,  $n(\mathbf{r})$ , is related to a set of Kohn-Sham electron orbitals [11]:

$$n(\mathbf{r}) = \sum_i |\phi_i(\mathbf{r})|^2. \quad (2.4)$$

Minimization of the functional above, while conserving the number of electrons, is equivalent to solving the self-consistent set of equations:

$$\left( T + V_0(\mathbf{r}) + \int d\mathbf{r}' \frac{n(\mathbf{r}')}{|\mathbf{r} - \mathbf{r}'|} + \frac{\delta E_{XC}[n]}{\delta n(\mathbf{r})} \right) \phi_i(\mathbf{r}) = E_i \phi_j(\mathbf{r}), \quad (2.5)$$

where the first term is the single-particle kinetic-energy operator. There are no known means to determine the exchange-correlation functional exactly. In this work, the form is

approximated as a local-density functional:

$$E_{XC}[n] = \int d^3\mathbf{r} n(\mathbf{r}) \epsilon_{XC}(n(\mathbf{r})), \quad (2.6)$$

where  $\epsilon_{XC}(n)$  is the exchange-correlation energy per electron in a uniform gas with density  $n$ . The exchange contribution to  $\epsilon_{XC}$  is that which arises from a Hartree-Fock calculation, and the correlation contribution is the remaining energy which can be obtained through the optimization of more complicated many-body states. The correlation energy has been parametrized for a range of electronic densities [12].

### 2.2.2 The Pseudopotential Approximation

Two considerations relevant to many crystals motivate the pseudopotential approximation. First, when electronic core states are relatively inert with respect to cohesive, bonding, and vibrational phenomena, an all-electron calculation can be limited to the case of isolated atoms, with modifications of the core states arising from the crystal field presumed negligible. Second, in many materials, particularly where valence states are  $s$  or  $p$  level and the potential they experience in the interstitial region is weak, the nearly-free electron approximation is useful and it is advantageous to work with a plane-wave basis.

In such situations, a pseudo Schrödinger equation can be written, where the valence states are replaced by pseudo states with correct eigenvalues, and the core-valence and nuclear-valence interactions are replaced by a pseudopotential. Not only is it then unnecessary to treat the core states within the solid, but serious computational problems in treating the effects of the strong potential near the nuclei can be avoided. This can be appreciated by recognizing that when using a plane-wave basis, for each electronic Bloch state, the Fourier components of the periodic ionic potential, corresponding to the reciprocal-lattice vectors, couple the plane waves with which it is expanded. This leads to a secular equation whose solution is equivalent to that of a matrix of size equal to the number of plane waves

retained. An estimation of how quickly the valence states must oscillate in order to attain orthogonality to the core state, and the magnitude of reciprocal lattice vectors which must enter the expansion as a consequence, quickly leads to the necessity of solving very large matrices.

On the other hand, by using pseudopotentials which generate valence states reproducing the actual orbitals outside the core region, possessing no radial nodes within it, and being well-matched at the boundary, the problem can be greatly simplified. In practice, methods are sought which result in the *transferability* of the pseudopotentials. This means that once a pseudopotential is calculated with respect to a *reference* valence configuration, the pseudo states it generates for other valence configurations meet the above criteria and have the correct scattering properties for a range of energies. Norm-conserving pseudopotentials [13] have been shown to meet these requirements. To do so, they generally need to act on valence angular-momentum components individually, and thus include nonlocal angular-momentum-dependent projectors as well as a local term. With these pseudopotentials, the density-functional procedure above is then carried out for the pseudized system. Below, the ground state is understood to be calculated accordingly. In this thesis, pseudopotentials were generated using Vanderbilt's cutoff functions [14] and separable Kleinman-Bylander non-local projectors [15] as modified in Ref. [16].

### 2.3 The Total Energy

Returning the nuclear coordinates to the problem, within the framework of density-functional theory and the pseudopotential approximation, the Born-Oppenheimer potential in Eq. 2.2 can be rewritten as

$$U_{B-O} = T + U_{nuc-el} + U_H + U_{XC} + U_{nuc-nuc}, \quad (2.7)$$

$$T = \frac{1}{2} \sum_i f_i \int d^3\mathbf{r} \phi_i^*(\mathbf{r}) (-\nabla^2) \phi_i(\mathbf{r}), \quad (2.8)$$

$$U_{nuc-el} = \sum_{i\tau\mathbf{R}} f_i \int d^3\mathbf{r} \phi_i^*(\mathbf{r}) \hat{v}_\tau(\mathbf{r} - \mathbf{R} - \mathbf{s}_\tau) \phi_i(\mathbf{r}), \quad (2.9)$$

and

$$U_{nuc-nuc} = \frac{N}{2} \sum_{\mathbf{R}\tau\tau'} \frac{Z_\tau Z_{\tau'}}{|\mathbf{R} + \mathbf{s}_\tau - \mathbf{s}_{\tau'}|} (1 - \delta_{\mathbf{R}0} \delta_{\tau\tau'}), \quad (2.10)$$

where  $\mathbf{R}$  is one of  $N$  Bravais lattice sites in the crystal, basis atoms are identified with the indices  $\tau$  and  $\tau'$ , and the corresponding basis vectors are  $\mathbf{s}_\tau$  and  $\mathbf{s}_{\tau'}$ . The third and fourth terms on the right of Eq. 2.7 are, respectively, the Hartree and exchange-correlation terms from Eq. 2.3, and  $\hat{v}_\tau(\mathbf{r} - \mathbf{R} - \mathbf{s}_\tau)$  is a pseudopotential. For clarity, the standard non-local part of the pseudopotential is suppressed here. Fermi occupation factors are indicated with  $f_i$  in the above expressions.

## 2.4 The Hellmann-Feynman Force Theorem

With the Hellmann-Feynman force theorem [17], forces on ions are seen to be a meaningful quantum-mechanical concept. Because the electronic orbitals are determined variationally, and their contribution to the total energy is stationary for fixed ionic positions, evaluation of the forces requires only terms in the total energy with explicit dependence on ion coordinates. If the Cartesian component,  $a$ , of an ionic position is given by  $r_{\tau a}(\mathbf{R}) = R_a + s_{\tau a} + x_{\tau a}(\mathbf{R})$ , with the final term representing the displacement from equilibrium, it follows that the force on the ion is [18]

$$F_{\tau a}(\mathbf{R}) = -\frac{\partial U_{nuc-el}}{\partial r_{\tau a}(\mathbf{R})} - \frac{dU_{nuc-nuc}}{dr_{\tau a}(\mathbf{R})}. \quad (2.11)$$

The angular-momentum-independent term in  $\partial U_{nuc-el}/\partial r_{\tau a}$  depends only on the charge density and local part of the pseudopotential, while projection operators between Kohn-Sham orbitals arise because of the angular-momentum-dependent term.



## Chapter 3

Phonon Dispersion Calculations: Si, Ge, diamond, and graphite.

### 3.1 Force Constants and the Dynamical Matrix

The inter-atomic force constants are defined by

$$C_{\tau\tau'ab}(\mathbf{R}) = \frac{\partial^2 V}{\partial x_{\tau a}(\mathbf{R}') \partial x_{\tau' b}(\mathbf{R} + \mathbf{R}')}, \quad (3.1)$$

where the simpler notation  $V = U_{B-O}$  is adopted for the Born-Oppenheimer energy surface,  $\mathbf{R}$  and  $\mathbf{R}'$  are lattice vectors, and  $x_{\tau a}(\mathbf{R})$  is the displacement from equilibrium of basis ion  $\tau$  at lattice vector  $\mathbf{R}$  along Cartesian direction  $a$ . The Fourier transformed, or Born-von Karman, force constants are

$$\tilde{\mathbf{C}}(\mathbf{k}) = \sum_{\mathbf{R}} \mathbf{C}(\mathbf{R}) e^{i\mathbf{k}\cdot\mathbf{R}}. \quad (3.2)$$

The above transformation manifests the equivalence among lattice sites which must be apparent in the dynamics of a system, which is symmetric with respect to lattice-vector translation.

The ionic masses,  $\{m_\tau\}$ , relate the Born-von Karman force constants to the dynamical matrix:

$$D_{\tau\tau'ab}(\mathbf{k}) = \frac{1}{\sqrt{m_\tau m_{\tau'}}} \tilde{C}_{\tau\tau'ab}(\mathbf{k}). \quad (3.3)$$

With  $n_\tau$  ions in the basis, the  $3Nn_\tau$  degrees of freedom of the crystal are spanned by the  $3Nn_\tau$  vibrational modes which diagonalize the dynamical matrix, with eigenvalues given by the mode frequencies squared, at  $N$  wave vectors. In the harmonic approximation, the modes are noninteracting oscillators. The independent oscillators then form the Fock space with which an arbitrary state of the crystal can be conveniently expressed. The quanta associated with such oscillators are phonons.

## 3.2 Calculating the Dynamical Matrix

The method described here proceeds in two steps: first, a set of high-symmetry wave vectors  $\{\mathbf{k}\}$  is chosen, and the corresponding Born-von Karman force constants,  $\{\tilde{\mathbf{C}}(\mathbf{k})\}$  are computed; and second, the counterpart inter-atomic force matrices are extracted through a least-squares fit, which minimizes the difference between the two sides of Eq. 3.2. Details of this procedure are provided in the Appendix. A fit is performed, rather than the familiar Fourier transform, to conveniently accommodate an irregular wave-vector grid while abiding by crystal symmetry. With the present treatment there is freedom to select the wave-vector grid, provided that the corresponding periodicities are commensurate with carefully chosen supercells.

The fit is performed subject to Eq. 3.2, together with the acoustic sum rule. Once the inter-atomic force constants are known, Eq. 3.2 determines the Born-von Karman force constants and the dynamical matrix at any wave vector within the Brillouin zone.

### 3.2.1 Sampling the Brillouin Zone

The periodic ionic displacements entering a frozen-phonon calculation are constructed with supercells, which can be larger than the primitive cell. In particular, cells are constructed such that ionic positions are given by

$$r_{\tau a}(\mathbf{R}) = R_a + s_{\tau a} + d_{\tau a} \cos(\mathbf{k} \cdot \mathbf{R}). \quad (3.4)$$

Above, the displacement from equilibrium,  $x_{\tau a}(\mathbf{R}) = d_{\tau a} \cos(\mathbf{k} \cdot \mathbf{R})$ , is written to represent a standing wave of wave vector  $\mathbf{k}$ . As an illustration, considering constructions four times the size of the primitive cell or smaller, the face-centered cubic lattice can be generated by supercells corresponding to inequivalent wave vectors along the following Cartesian directions:  $(1, 0, 0)$ ,  $(1, 1, 1)$ ,  $(1, 1, 0)$ ,  $(2, 1, 0)$  and  $(3, 3, 1)$ . Lower-symmetry wave-vectors can be represented with larger supercells. The Hellmann-Feynman force is computed as described

in the previous chapter.

The harmonic approximation implies that the forces and force constants are related by

$$\begin{aligned} F_{\tau a}(\mathbf{R}'') &= -\sum_{\mathbf{R}'\tau'b} C_{\tau\tau'ab}(\mathbf{R}' - \mathbf{R}'') x_{\tau'b}(\mathbf{R}') \\ &= -\sum_{\mathbf{R}'\tau'b} C_{\tau\tau'ab}(\mathbf{R}') d_{\tau'b} \cos(\mathbf{k}\cdot(\mathbf{R}'' + \mathbf{R}')), \end{aligned} \quad (3.5)$$

where  $\mathbf{R}'$  is shifted, and the ionic displacements from equilibrium are substituted from Eq. 3.4. If  $d_{\tau'b}$  is nonzero for only a single ion  $\tau'$  and direction  $b$ , and is varied over two successive electronic calculations, the following demonstrates that the finite difference in Hellmann-Feynman forces can be related directly to the dynamical matrix. Starting with

$$\frac{\partial F_{\tau a}(\mathbf{R}'')}{\partial d_{\tau'b}} = -\sum_{\mathbf{R}'} C_{\tau\tau'ab}(\mathbf{R}') \cos(\mathbf{k}\cdot(\mathbf{R}'' + \mathbf{R}')), \quad (3.6)$$

and using the basic identity

$$\cos(a + b) = \cos(a) \cos(b) - \sin(a) \sin(b)$$

and Eq. 3.2, we obtain

$$\begin{aligned} \text{Re}(\tilde{C}_{\tau\tau'ab}(\mathbf{k})) &= -\frac{1}{2 \cos(\mathbf{k}\cdot\mathbf{R}'')} \left( \frac{\partial F_{\tau a}(\mathbf{R}'')}{\partial d_{\tau'b}} + \frac{\partial F_{\tau a}(-\mathbf{R}'')}{\partial d_{\tau'b}} \right) \\ \text{Im}(\tilde{C}_{\tau\tau'ab}(\mathbf{k})) &= \frac{1}{2 \sin(\mathbf{k}\cdot\mathbf{R}'')} \left( \frac{\partial F_{\tau a}(\mathbf{R}'')}{\partial d_{\tau'b}} - \frac{\partial F_{\tau a}(-\mathbf{R}'')}{\partial d_{\tau'b}} \right). \end{aligned} \quad (3.7)$$

The lattice vector  $\mathbf{R}''$  is arbitrary, but chosen within the supercell such that the denominator is nonzero. In the case that  $\mathbf{k}$  is along certain high-symmetry directions and is half of a reciprocal-lattice vector,  $\mathbf{k}\cdot\mathbf{R}''$  is a multiple of  $\pi$  for all  $\mathbf{R}''$ . At these points the condition  $\tilde{C}(\mathbf{k}) = \tilde{C}(-\mathbf{k})$  is valid, and by Eq. 3.2, the equality  $\tilde{C}(\mathbf{k}) = (\tilde{C}(-\mathbf{k}))^*$  follows, demonstrating that the reciprocal-space matrix must be purely real at any such point.

The practical result of Eq. 3.7 is that an entire row of the reciprocal-space matrix is known from two calculations, each equivalent to a supercell calculation of total energy. Typically, knowledge of the Born-von Karman force constants at two or three wave vectors

along each high-symmetry direction is sufficient for a good phonon dispersion throughout the BZ. The sampled matrices, which are calculated directly with a calculation of the electronic ground state, incorporate interactions between ions which are not local to the supercell, by virtue of its wave commensurability. However the interpolated matrices, to be discussed below, are evaluated by introducing real-space cutoffs. While the standard approximations to the electronic ground state are present in the calculated dynamical matrices, through construction of supercells representing standing waves mapped to the BZ point considered, Eq. 3.7 formally accounts for all the forces. This characteristic of the scheme distinguishes it from the typical frozen-phonon techniques found in the literature.

In order to carry out the interpolation of the dynamical matrix, a discrete Fourier transform on the complete set of vectors within a parallelepiped box may appear tempting. If one wishes to respect the symmetry of the crystal, however, this tactic will not work. Generally, the set of vectors spanned by such a box will include some vectors within a symmetry-related subset, and not others. If the set is inclusive enough, the artificial asymmetry introduced may be negligible, because  $\mathbf{C}(\mathbf{R})$  is expected to diminish reasonably quickly with  $\mathbf{R}$ , and the set can include all members of any subset whose components have significant magnitude.

Rather than performing a Fourier transform, by overdetermining the inter-atomic force constants used in Eq. 3.2 and then performing a least-squares fit, the crystal symmetry is preserved here, and no nuisance is posed by the choice of wave-vector sampling. The following section details how this procedure is implemented. Key features of the formulation are that all symmetries of the crystal are respected, the symmetries are exploited to minimize the number of parameters to be fit, and frequencies of the acoustic phonons are guaranteed to go to zero in the limit of small wave vector.

The next section assumes that the real-space matrices are short-ranged, and do not include the long-range Coulombic, ion-ion interactions. As a result, the treatment, without

being supplemented, can be applied only to nonpolar crystals, such as Si. The subsequent chapter extracts the contributions from the Coulombic interactions and extends the formalism to polar crystals.

### 3.2.2 Interpolation

The number of independent force constants can be reduced with application of the operations comprising the crystal's symmetry group. The set of such operations are indicated by  $\mathbf{U}_n$ , and may include a non-zero glide,  $\mathbf{g}_n$ .

We may indicate the paired basis ions  $\tau$  and  $\tau'$ , at relative lattice vector separation  $\mathbf{R}$ , with the notation:  $(\mathbf{R}, \tau, \tau')$ . If the conditions,

$$\mathbf{U}_n \mathbf{s}_\tau = \mathbf{s}_\sigma + \mathbf{g}_n + \mathbf{R}(\mathbf{U}_n, \mathbf{s}_\tau),$$

$$\mathbf{U}_n \mathbf{s}_{\tau'} = \mathbf{s}_{\sigma'} + \mathbf{g}_n + \mathbf{R}(\mathbf{U}_n, \mathbf{s}_{\tau'}),$$

and

$$\mathbf{R}' = \mathbf{U}_n \mathbf{R} + \mathbf{R}(\mathbf{U}_n, \mathbf{s}_{\tau'}) - \mathbf{R}(\mathbf{U}_n, \mathbf{s}_\tau), \quad (3.8)$$

are met, the ion pairs  $(\mathbf{R}, \tau, \tau')$  and  $(\mathbf{R}', \sigma, \sigma')$  are symmetry equivalent. The transformation of the force constants can be conveniently discussed by decomposing them into  $3 \times 3$  elements,  $\mathbf{C}_{\tau\tau'}(\mathbf{R})$ , corresponding to the force constants between the ion pairs indicated above. The transformations are,

$$(\mathbf{U}_n \mathbf{e}_a)^T \cdot \mathbf{C}_{\sigma\sigma'}(\mathbf{R}') \cdot (\mathbf{U}_n \mathbf{e}_b) = \mathbf{e}_a^T \cdot \mathbf{C}_{\tau\tau'}(\mathbf{R}) \cdot \mathbf{e}_b. \quad (3.9)$$

The corresponding Born-von Karman transformations are,

$$\tilde{\mathbf{C}}_{\sigma\sigma'}(\mathbf{U}_n \mathbf{k}) = \exp(i\mathbf{k} \cdot (\mathbf{s}_\tau - \mathbf{s}_{\tau'} - \mathbf{U}_n^{-1}(\mathbf{s}_\sigma - \mathbf{s}_{\sigma'}))) \mathbf{U}_n^{-1} \tilde{\mathbf{C}}_{\tau\tau'}(\mathbf{k}) \mathbf{U}_n. \quad (3.10)$$

The force constants must also satisfy the condition

$$\mathbf{C}_{\tau'\tau}^T(-\mathbf{R}) = \mathbf{C}_{\tau\tau'}(\mathbf{R}). \quad (3.11)$$

With the above relations, the number of independent force constants is reduced, and it can be deduced that many are zero.

With the reduced set of non-zero force constants, the select dynamical matrices calculated via the Hellmann-Feynman forces, and Eq. 3.3, a least-squares fit may be performed to extract the optimal  $\mathbf{C}_{\tau\tau'}(\mathbf{R})$  for all the ion pairs subject to some cutoff:  $\|\mathbf{R} + \mathbf{s}_\tau - \mathbf{s}_{\tau'}\| < r_c$ . To enforce the acoustic sum rule, which guarantees acoustic phonon frequencies approach zero at small wave vector, the fit is constrained so that it meets the condition

$$\sum_{\mathbf{R}\tau'} [\mathbf{C}_{\tau\tau'}(\mathbf{R})]_{ab} = 0, \quad (3.12)$$

where the sum is over all the ion pairs included within the cutoff. The above condition is equivalent to translation invariance of the crystal, and can be motivated by analogy with the form of a two-body harmonic force matrix, which depends on the relative coordinate, and is independent of the center-of-mass coordinate.

### 3.3 Computational Details

Dispersion curves and phonon densities of states for diamond, Ge, Si and graphite are presented in the figures. Below are listed which phonon  $\mathbf{k}$  points are used in each fit, and which real-space triplet matrices are included. These particular selections are somewhat arbitrary, so long as the BZ is adequately sampled and the triplet matrices are overdetermined. For the case of graphite, extra weight is given to the  $\Gamma$  point in the fit to ensure that at very small  $\mathbf{k}$  the very small eigenvalues of the dynamical matrix,  $\omega^2$ , do not go negative.

The symmetries are determined from lattice structure: for Si, Ge, and diamond, the primitive lattice vectors are

$$\mathbf{a}_1 = \frac{a}{2}(0, 1, 1), \quad \mathbf{a}_2 = \frac{a}{2}(1, 0, 1), \quad \mathbf{a}_3 = \frac{a}{2}(1, 1, 0).$$

A lattice constant of  $10.05 a_0$  is employed for Si,  $10.34 a_0$  for Ge, and  $6.68 a_0$  for diamond (all reported lattice constants correspond to the values for the theoretically relaxed crystals).

For the diamond-type crystals, the two basis sites are symmetry-mapped. The basis vectors for each crystal can be written,

$$\mathbf{s}_{\tau_1} = -\frac{1}{8}(\mathbf{a}_1 + \mathbf{a}_2 + \mathbf{a}_3), \quad \mathbf{s}_{\tau_2} = \frac{1}{8}(\mathbf{a}_1 + \mathbf{a}_2 + \mathbf{a}_3).$$

The lattice vectors of graphite are:

$$\mathbf{a}_1 = a \left( \frac{\sqrt{3}}{2}, \frac{1}{2}, 0 \right), \quad \mathbf{a}_2 = a \left( \frac{\sqrt{3}}{2}, -\frac{1}{2}, 0 \right), \quad \mathbf{a}_3 = c(0, 0, 1),$$

the in-plane lattice constant is  $4.88 a_0$ , and the lattice parameters take the ratio,  $c/a = 2.72$ .

The basis for graphite is

$$\mathbf{s}_{\tau_1} = \frac{1}{4}\mathbf{a}_3, \quad \mathbf{s}_{\tau_2} = -\frac{1}{4}\mathbf{a}_3, \quad \mathbf{s}_{\tau_3} = -\frac{1}{3}(\mathbf{a}_1 + \mathbf{a}_2) + \frac{1}{4}\mathbf{a}_3, \quad \mathbf{s}_{\tau_4} = \frac{1}{3}(\mathbf{a}_1 + \mathbf{a}_2) - \frac{1}{4}\mathbf{a}_3.$$

For diamond, the  $\mathbf{k}$  points included in the fit are  $\Gamma$ ,  $\mathbf{X}$ ,  $\mathbf{L}$ ,  $\mathbf{K}$ ,  $\frac{2}{3}\mathbf{X}$ ,  $\frac{2}{3}\mathbf{L}$ ,  $\frac{1}{2}\mathbf{X}$ ,  $\frac{1}{2}\mathbf{L}$ ,  $\frac{3}{4}\mathbf{K}$ ,  $\mathbf{W}$ , using cubic convention, and the lower-symmetry point  $(2\pi/a)(1/4, 3/4, -3/4)$ .

The prototypical triplets are the basis pairs  $(\tau_1 \tau_1)$  and  $(\tau_1 \tau_2)$  for  $\mathbf{R} = (0, 0, 0)$ ;  $(\tau_1 \tau_1)$  and  $(\tau_1 \tau_2)$  for  $\mathbf{R} = -\mathbf{a}_1$ ;  $(\tau_1 \tau_2)$  for  $\mathbf{R} = \mathbf{a}_1 - \mathbf{a}_3$ ;  $(\tau_1 \tau_1)$  and  $(\tau_1 \tau_2)$  for  $\mathbf{R} = \mathbf{a}_3 - \mathbf{a}_2 - \mathbf{a}_1$ ;  $(\tau_1 \tau_1)$  and  $(\tau_1 \tau_2)$  for  $\mathbf{R} = 2\mathbf{a}_3 - \mathbf{a}_2 - 2\mathbf{a}_1$ ;  $(\tau_1 \tau_2)$  for  $\mathbf{R} = 2\mathbf{a}_1 - \mathbf{a}_2 - \mathbf{a}_3$ ; and  $(\tau_1 \tau_1)$  for  $\mathbf{R} = -2\mathbf{a}_1$ .

All triplets symmetry-related to those within the prototypical set enter the computation, so that altogether 246 triplets are accounted.

Additional interactions and phonons are included in the studies of Si and Ge. In these systems, wave-vector sampling is extended to the lower-symmetry points:  $(2\pi/a)(3/5, 1, -7/5)$  and  $(2\pi/a)(-3/5, 1, -1/5)$ . For Ge, triplet interactions  $(\tau_1 \tau_1)$  for  $\mathbf{R} = \mathbf{a}_3 - \mathbf{a}_2 - 2\mathbf{a}_1$  and those related are considered along with the set listed for diamond, for a total of 294 triplets. For Si, the additional interactions related to the triplet  $(\tau_1 \tau_2)$  for  $\mathbf{R} = \mathbf{a}_1 + \mathbf{a}_2$  are retained, for a total of 318 triplets.

The graphite calculation includes the phonons at  $\Gamma$ ,  $\mathbf{K}$ ,  $\mathbf{M}$ ,  $\mathbf{A}$ ,  $\mathbf{W}$ ,  $\frac{2}{3}\mathbf{M}$ ,  $\frac{1}{2}\mathbf{M}$ , and  $\frac{3}{4}\mathbf{K}$ . The graphite triplets are: the pairs  $(\tau_1 \tau_1)$ ,  $(\tau_1 \tau_2)$ ,  $(\tau_1 \tau_3)$ ,  $(\tau_1 \tau_4)$ ,  $(\tau_3 \tau_3)$ , and  $(\tau_3 \tau_4)$  for

$\mathbf{R} = (0, 0, 0)$ ; the pairs  $(\tau_1\tau_1)$ ,  $(\tau_1\tau_2)$ ,  $(\tau_1\tau_3)$ ,  $(\tau_3\tau_3)$ , and  $(\tau_3\tau_4)$  for  $\mathbf{R} = -\mathbf{a}_1$ ; the pairs  $(\tau_1\tau_3)$  and  $(\tau_2\tau_4)$  for  $\mathbf{R} = \mathbf{a}_1 - \mathbf{a}_2$ ; and the pairs  $(\tau_1\tau_1)$ , and  $(\tau_3\tau_3)$ , for  $\mathbf{R} = \mathbf{a}_2 - 2\mathbf{a}_1$ .

Different parameter sets were employed in the Si and Ge calculations as a check on the robustness of the results with respect to these choices. With the wave-commensurate method, there is some inherent limitation to wave-vector sampling, which in turn limits the number of inter-atomic force constants which can be retained. Ultimately, the sufficient nature of the parameter sets adopted in these calculations is evaluated by a comparison of the present results with experimental values, described above. Below, the fitting procedure's contribution to the uncertainty is analyzed. The uncertainties associated with parameter choices is closely related to those of the fitting procedure. For instance, with ideal sampling and inter-atomic force constant inclusion, the fitting procedure would not be a significant source of error.

### 3.4 Uncertainties and Comparison with Experiment

The phonon frequencies calculated are convergent to 1 % or better with respect to the computational parameters. These include the number of electronic states within the Brillouin zone sampled in evaluating the total energy and Hellmann-Feynman forces, and the number of plane waves retained in the expansion. For the Brillouin zone sampling, a 4x4x4 grid is sufficient, and for the plane waves, a cutoff corresponding to an electronic kinetic energy of 16 Ry is sufficient for Si and Ge, and 49 Ry for the carbon systems, diamond and graphite. The convergence of the calculations with respect to these parameters was checked by increasing sampling and plane-wave cutoff. The sensitivity was seen to be negligible compared to the below-discussed sources of error and uncertainty.

The two most evident sources of error and uncertainty in the quantities reported here are those relating to the theoretical equilibrium volumes at which the lattice dynamical calculations are performed, and the fitting procedure. The lattice constant calculated is 2 %



lower than the measured value for Si, 1 % lower for diamond and 3 % lower for Ge [19, 20]. When phonon frequencies are calculated at the  $\Gamma$  and  $\mathbf{X}$  points with the experimental volume, the phonon frequencies are reduced by more than 5 % for these materials. The equilibrium volumes for the diamond-type materials are determined by performing total-energy calculations for a range of volumes, and then fitting the results to the Murnaghan equation of state [21]. For graphite, the equilibrium volume is determined through minimization of the total energy with a variation over two parameters: the volume and the ratio,  $c/a$ .

A comparison of the mode frequencies derived from the electronic calculations, and those returned by the interpolation, reveals another significant source of error. While the difference for the majority of modes is less than 5 %, for a few of the acoustic modes the difference is nearly 15 %. The largest difference between calculated and interpolated frequency at any mode is approximately 6 % of the  $TO(\Gamma)$  mode frequency.

For diamond, when compared with experiment, the theoretical phonon frequency is 1 % too large for the mode  $TO(\Gamma)$ , 6 % too large for  $L(\mathbf{X})$ , 6 % too small for  $TO(\mathbf{X})$ , and 4 % too small for  $TA(\mathbf{X})$  [22]. For Si, the theoretical frequency is 3 % too large for the mode  $TO(\Gamma)$ , 9 % too small for  $L(\mathbf{X})$ , 7 % too large for  $TO(\mathbf{X})$ , and 34 % too large for  $TA(\mathbf{X})$  [23]. For Ge, the theoretical frequencies agree with experiment to 1 % or better for all above modes except for the mode  $TA(\mathbf{X})$ , for which the theoretical value is 7 % too large [23, 24].

Theoretical elastic constants for Ge are  $c_{11} = 116$  GPa and  $c_{44} = 92.6$  GPa, approximately 10 % smaller and 45 % higher than the measured values, respectively [25]. For Si, the values are  $c_{11} = 190$  GPa and  $c_{44} = 93.2$  GPa, each about 20 % larger than the experimentally determined values [25]. For diamond, the values are  $c_{11} = 1230$  GPa and  $c_{44} = 507$  GPa, approximately 15 % too large and 15 % too small, respectively [20]. Although  $c_{12}$  can be evaluated through an analysis of the three independent speeds of sound

along the  $\mathbf{k} = (110)$  direction, the analysis was not performed in this work.

The calculated bond lengths for graphite are approximately 5 % larger than the measured value, but the ratio agrees with the experimental ratio to better than 1 % [26]. The three largest-frequency modes calculated at  $\Gamma$  are, in order of energy, 3 % larger, 1 % smaller, and 20 % smaller than experiment [27].

Inspection of the phonon dispersions and state densities reveals the expected similarities between the results for Si and Ge, where the inter-atomic forces are very similar. In contrast, in diamond, the transverse acoustic mode energies—relative to the other branches—are greater than in the above materials.

The greatest disparity from experimental dispersion is for the low-lying transverse acoustic modes. The numerical difficulty associated with the flattening of the transverse acoustic branch as the zone boundary is approached may contribute to this difficulty. A greater density of wave-vector sampling may improve these results.

As these results represent the calculation of a state continuum, different approximations have varying impacts on the different states. The acceptability of any calculation depends on the particular quantity of interest.

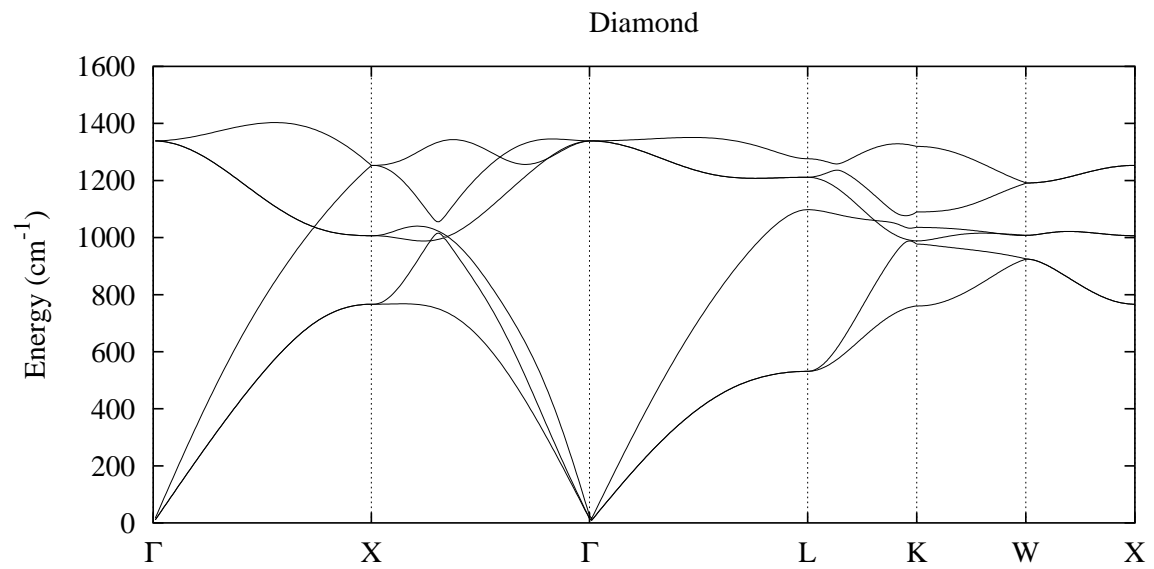


Figure 3.1: Calculated phonon dispersion in diamond.

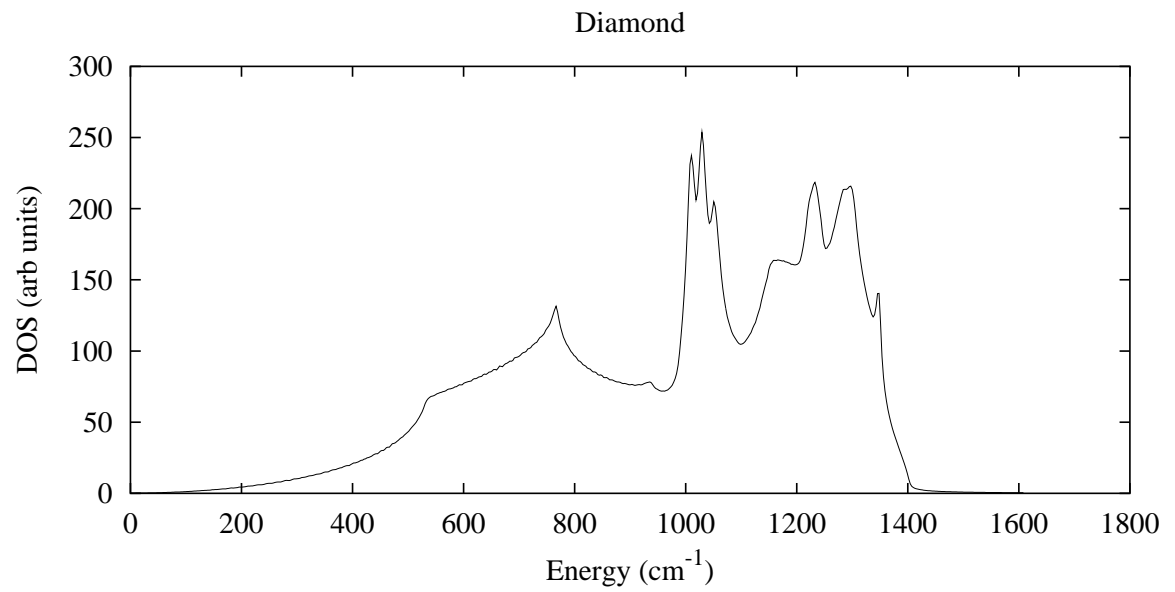


Figure 3.2: Calculated phonon density of states in diamond.

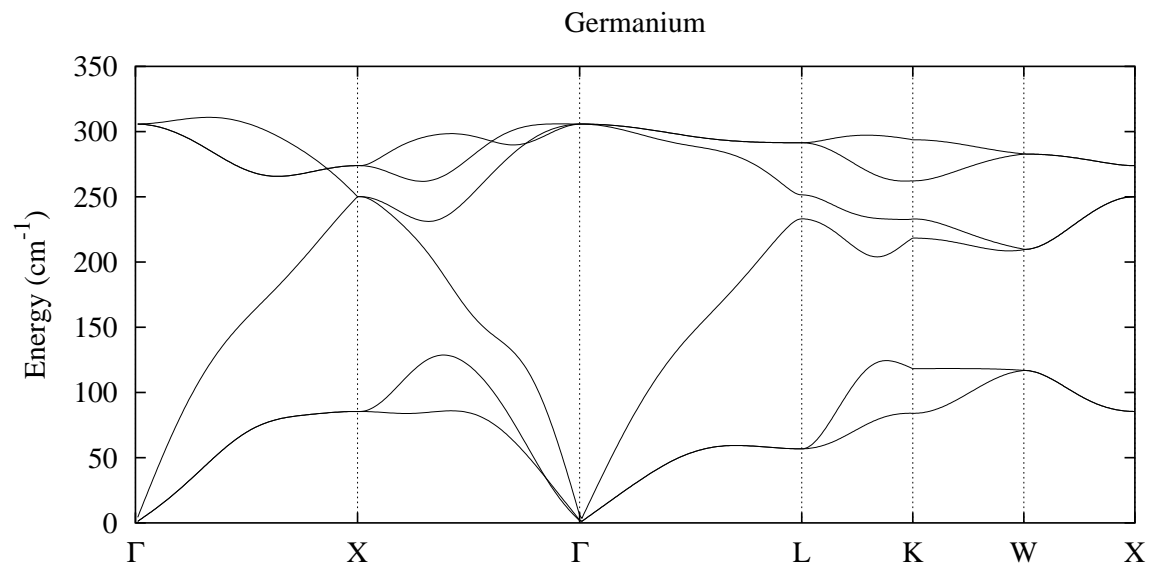


Figure 3.3: Calculated phonon dispersion in Ge.

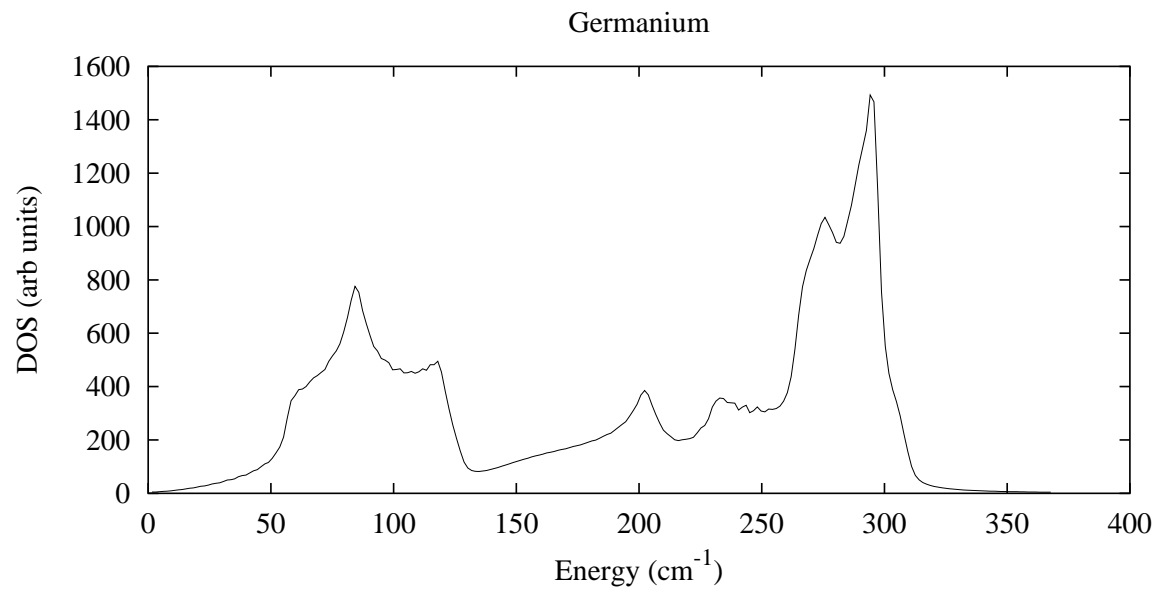


Figure 3.4: Calculated phonon density of states in Ge.

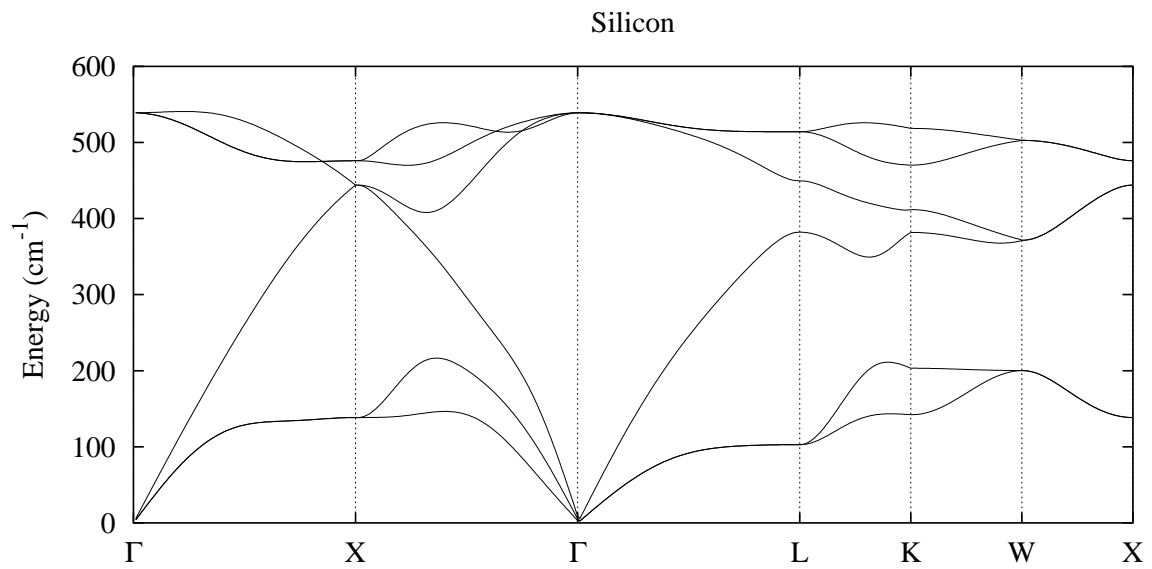


Figure 3.5: Calculated phonon dispersion in Si.

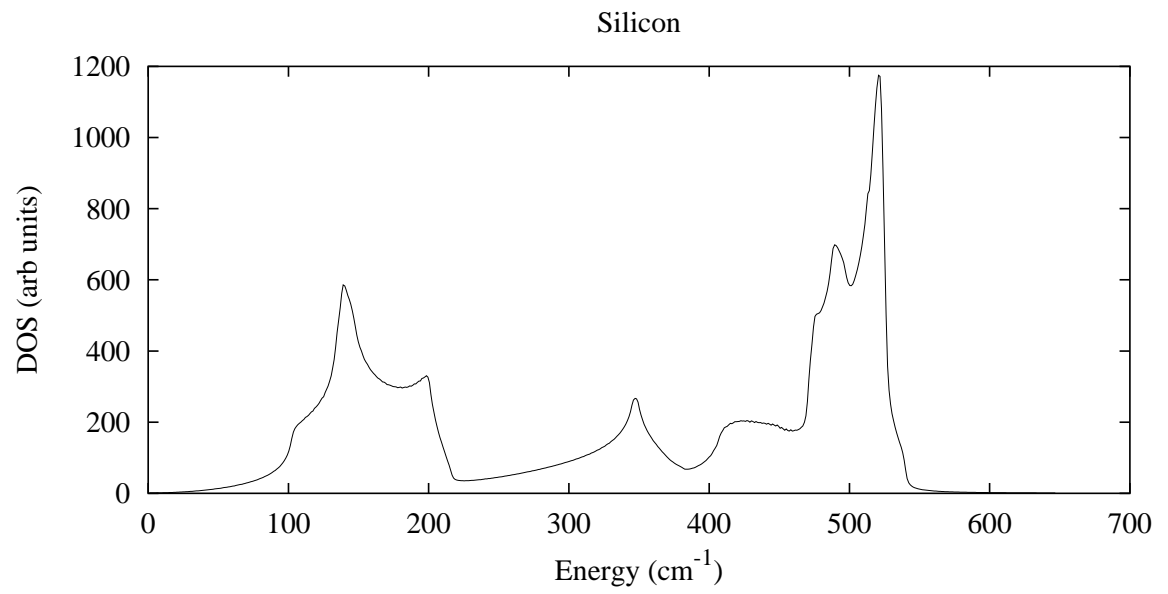


Figure 3.6: Calculated phonon density of states in Si.



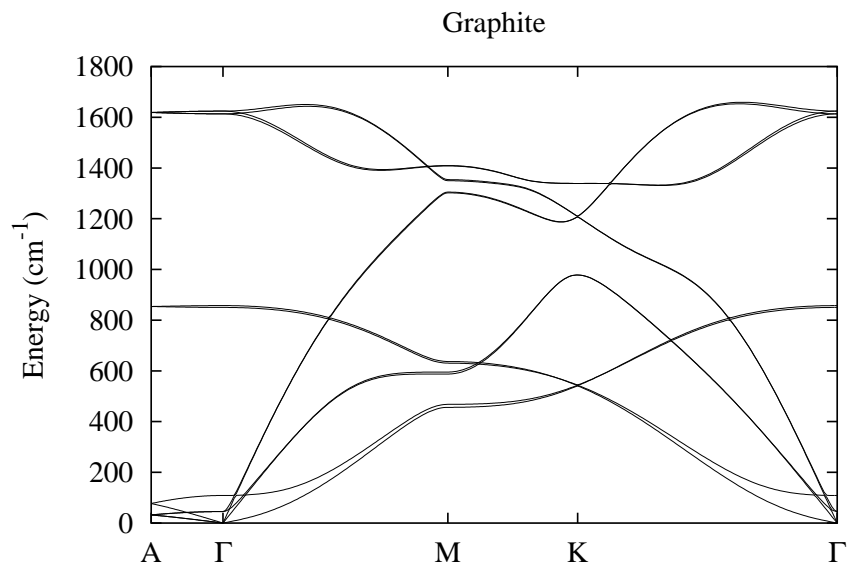


Figure 3.7: Calculated phonon dispersion in graphite.

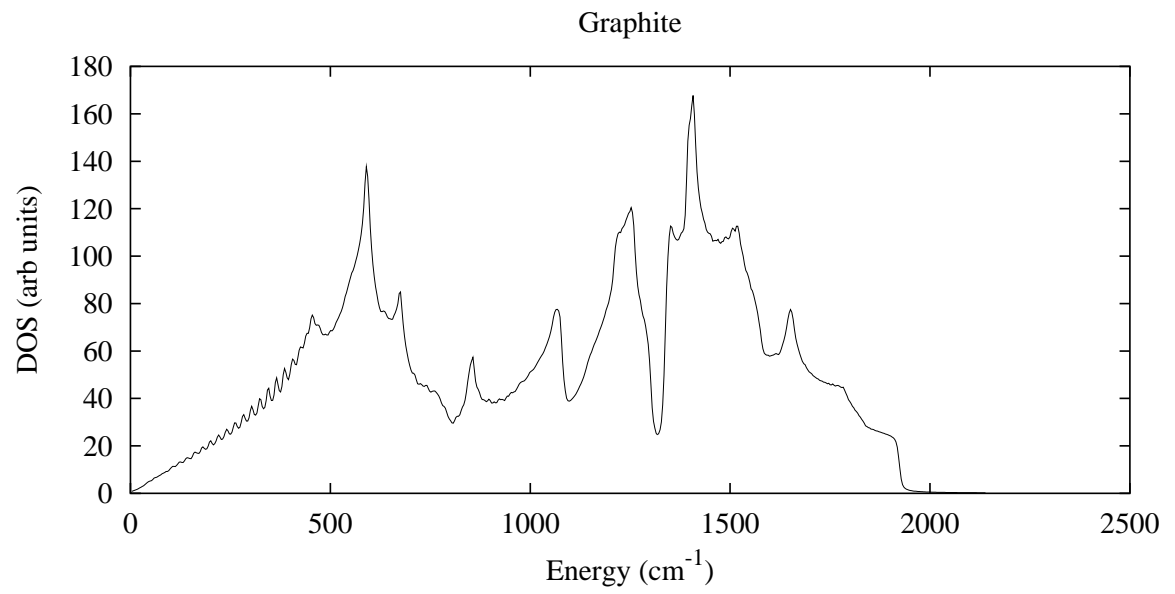


Figure 3.8: Calculated phonon density of states in graphite.

## Chapter 4

### Polar Crystals: GaAs and GaP

#### 4.1 Macroscopic Fields: Phonon Dispersion and Infrared Response

All of the discussion of the preceding chapter assumes boundary conditions which are periodic with respect to the volume of a primitive cell in the crystal. An immediately apparent violation of this condition is the presence of a macroscopic electric field, whose average over a primitive cell in the crystal is nonzero.

In fact, light quanta which are of similar energy to the phonons have wavelengths much greater than a lattice constant, and so consideration of the infrared response requires a theoretical account of macroscopic fields. Further, in crystals which do not obey an inversion-symmetry invariance, long-wavelength phonons are accompanied by macroscopic fields when the phonon polarizations are longitudinal. Thus, small-momentum longitudinal and transverse modes are not degenerate. It may not be surprising, and will be shown below, that the longitudinal-transverse energy difference is closely related to the infrared response. This thesis studies these effects in the polar, type III-IV materials GaAs and GaP.

The Hamiltonian density for a polar crystal in the presence of an electric field,  $\mathbf{E}$ , can be written as [28]

$$H = \sum_{\lambda} \frac{1}{2N\Omega} (\omega_{\lambda}^2 q_{\lambda}^2 + \dot{q}_{\lambda}^2) - \mathbf{E} \cdot \mathbf{P}^{lat} + \frac{1}{8\pi} \varepsilon_{\infty} \mathbf{E} \cdot \mathbf{E}. \quad (4.1)$$

The normal coordinate and frequency, respectively, of a phonon with wave vector and branch indexed by  $\lambda$  are indicated by  $q_{\lambda}$  and  $\omega_{\lambda}$ . For the long-wave modes, the restoring frequencies above correspond to those of transverse polarization. These frequencies are obtained from an electronic calculation satisfying periodic boundary conditions over a unit cell. It will be shown below that the physical frequencies must be modified when considering the longitu-

dinal modes, because of coupling between the macroscopic lattice polarization and electric field.  $\mathbf{P}^{lat}$  is the lattice contribution to the macroscopic polarization, and its dimensions are dipole moment per unit volume. The unit cell volume is  $\Omega$  and the number of Bravais lattice sites is  $N$ . The electronic dielectric constant of the crystal,  $\varepsilon_\infty$ , may be considered to be a scalar for the materials studied here. Because the primary focus of this work is lattice dynamics, the indices related to ionic motion will, for the moment, be retained.

The lattice contribution to the macroscopic polarization in Eq. 4.1 can be written as,

$$P_i^{lat} = \frac{1}{\Omega} \sum_\nu \sum_{\tau j} \frac{1}{\sqrt{m_\tau}} Z_{ij}^\tau q_\nu \epsilon_{\tau j}^\nu. \quad (4.2)$$

In the above,  $m_\tau$  is the mass of ion  $\tau$ , the phonon normal coordinate index,  $\nu$ , runs strictly over the zero-momentum phonons, and  $\epsilon_{\tau j}^\nu$  is a component of the polarization of such a phonon. Cartesian directions are indicated with the indices  $i$  and  $j$ . The charges are expressed as the change in macroscopic polarization with respect to sublattice displacement:

$$Z_{ij}^\tau = \Omega \frac{\partial P_i^{lat}}{\partial u_{\tau j}}. \quad (4.3)$$

Subtleties in the interpretation and calculation of  $Z_{ij}^\tau$  are discussed below.

Substituting Eq. 4.2 into Eq. 4.1 the following driven-oscillator solution for the phonon normal coordinate equation of motion is obtained,

$$q_\nu(\omega) = \sum_{\tau' i' j'} \left( \frac{1}{\omega_\nu^2 - \omega^2} \right) \frac{Z_{i' j'}^{\tau'} \epsilon_{\tau' j'}^\nu E_{i'}(\omega)}{\sqrt{m_{\tau'}}}. \quad (4.4)$$

It follows that the total polarization is:

$$P_i(\omega) = \frac{1}{\Omega} \sum_\nu \sum_{\tau \tau' i' j j'} \left( \frac{1}{\omega_\nu^2 - \omega^2} \right) \frac{Z_{ij}^\tau Z_{i' j'}^{\tau'} \epsilon_{\tau j}^\nu \epsilon_{\tau' j'}^\nu E_{i'}(\omega)}{\sqrt{m_\tau m_{\tau'}}} + \frac{\varepsilon_\infty - 1}{4\pi} E_i(\omega), \quad (4.5)$$

so that the dielectric function is written [28],

$$\varepsilon_{ii'}(\omega) = \delta_{ii'} \varepsilon_\infty + \frac{4\pi}{\Omega} \sum_\nu \left( \frac{1}{\omega_\nu^2 - \omega^2} \right) \sum_{\tau \tau' j j'} \frac{Z_{ij}^\tau Z_{i' j'}^{\tau'} \epsilon_{\tau j}^\nu \epsilon_{\tau' j'}^\nu}{\sqrt{m_\tau m_{\tau'}}}, \quad (4.6)$$

which is a well-known result.

In a zincblende crystal, the charge tensors, as well as the electronic dielectric function, are proportional to the identity matrix and are expressed as

$$\varepsilon_{ii'}(\omega) = \delta_{ii'}\varepsilon(\omega). \quad (4.7)$$

This allows Eq .4.6 to be written as,

$$\varepsilon(\omega) = \varepsilon_\infty + \frac{4\pi Z^2}{\Omega\mu} \left( \frac{1}{\omega_{TO}^2 - \omega^2} \right), \quad (4.8)$$

where  $\mu$  is the basis-ion reduced mass. This is the case considered below.

Maxwell's equations require the condition  $\nabla \cdot \mathbf{D} = 0$  within a bulk dielectric. This, combined with the above equations, implies

$$\mathbf{k} \cdot \left( \varepsilon_\infty + \frac{4\pi}{\Omega} \left( \sum_{\nu\tau\tau'} \frac{Z_{ii}^\tau Z_{ii}^{\tau'} \varepsilon_{\tau i}^\nu \varepsilon_{\tau' i}^\nu}{\sqrt{m_\tau m_{\tau'}} (\omega_\nu^2 - \omega^2)} \right) \right) \mathbf{E} = 0, \quad (4.9)$$

where the  $\omega_\nu$  in the absence of the macroscopic fields are implied to be degenerate, and  $\mathbf{k}$  is the simultaneous wave vector of the electric field and lattice displacement field. Note, as discussed above, the dielectric function in Eq. 4.9 is expressed as a scalar.

Plainly, transverse fields—such as the TO phonon, and coupled TO-phonon-photon modes, or polaritons—will always satisfy Eq. 4.9. The physical frequencies of the long-wave, longitudinal modes are derived by looking for solutions of Eq. 4.9 without requiring the condition  $\mathbf{k} \cdot \mathbf{E} = 0$ . Denoting such a frequency

$$\omega = \omega_{LO}, \quad (4.10)$$

and combining Eq. 4.9 with Eq. 4.6, the Lyddane-Sachs-Teller [29] relation is obtained. The result is that the longitudinal frequency is related to the frequency appropriate to periodic boundary conditions by

$$\frac{\varepsilon(0)}{\varepsilon_\infty} = \frac{\omega_{LO}^2}{\omega_{TO}^2}, \quad (4.11)$$

and we identify the latter with transverse displacements.

## 4.2 The Modern Theory of Polarization and Calculation of the Born Effective Charges

The modern theory of polarization takes up the interpretation and calculation of a bulk solid's electrical response to some long-wave change in configuration, such as a strain. Classical approaches, such as the Clausius-Mossotti model, are insufficient in the presence of delocalized charge distributions. The ambiguities involved with evaluating dipoles in infinite systems with covalency may be anticipated, and it has been shown that Wannier transformations yield nonunique results depending on the nonobservable phases of the Bloch functions.

To overcome these difficulties, the modern theory of polarization disregards the polarization itself as an observable, and instead retains its change with respect to some adiabatic evolution. By shifting from the polarization to its change, appropriate expressions can be obtained which involve localized and neutral charge distributions, as in the Clausius-Mossotti model. The change is written [7]:

$$\Delta \mathbf{P} = \Delta \mathbf{P}_{ion} + \frac{2e}{\Omega} \sum_n \int d^3 \mathbf{r} \mathbf{r} (|a_n^{(1)}(\mathbf{r})|^2 - |a_n^{(0)}(\mathbf{r})|^2). \quad (4.12)$$

The electron Bloch bands are indexed by  $n$  above, the integral is over the primitive cell, and the Wannier functions are calculated from the Bloch Kohn-Sham orbitals [11]:

$$a_n^{(\lambda)}(\mathbf{r}) = \frac{\sqrt{\Omega}}{(2\pi)^3} \int d^3 \mathbf{q} \phi_n^\lambda(\mathbf{q}, \mathbf{r}). \quad (4.13)$$

The superscript represents a particular state along the adiabatic evolution. So long as there is a band gap, the above has been shown to be invariant with respect to the most general unitary transformations on the occupied states. For the Born effective charges, the adiabatic transformation appearing above is a sublattice displacement.

The electronic contribution to the component of polarization along a reciprocal lattice

vector,  $\mathbf{P} \cdot \hat{\mathbf{G}}$  is calculated with

$$\mathbf{P}^\lambda \cdot \hat{\mathbf{G}} = -\frac{e}{8\pi^3} \int d^2 \mathbf{k}_\perp \phi^\lambda(\mathbf{k}_\perp), \quad (4.14)$$

where the integral is performed over a surface in the parallelepiped Brillouin zone, normal to  $\mathbf{G}$ . The dimensionless phase,  $\phi^\lambda(\mathbf{k}_\perp)$ , is calculated through a line integral. The integral is taken through the point  $\mathbf{k}_\perp$ , parallel to  $\mathbf{G}$ , and in the continuous limit is written as,

$$\phi^\lambda(\mathbf{k}_\perp) = -i \sum_n \int dk \langle u_{\mathbf{k}\mathbf{n}}^\lambda | \frac{\partial}{\partial k} | u_{\mathbf{k}\mathbf{n}}^\lambda \rangle. \quad (4.15)$$

Above, the periodic part of the Bloch orbitals of band  $n$  and wave vector  $\mathbf{k}$  is indicated by  $u_{\mathbf{k}\mathbf{n}}^\lambda$ , and the integral is taken from 0 to  $|\mathbf{G}|$ . As discussed elsewhere, evaluation of the above expressions require additional care, because of ambiguities associated with the phases of  $u_{\mathbf{k}\mathbf{n}}^\lambda$ , and with band degeneracies and band crossing.

### 4.3 Phonon Dispersion and Macroscopic Fields

As mentioned, polar materials, in which distortions interior to the primitive cell can generate electric dipoles, require additional consideration for the calculation of phonon spectra. This is because the periodicity built into the electronic calculations will not accommodate a non-zero dipole over the supercell, and hence cannot capture any physics associated with macroscopic electric polarizations or fields. As we have seen, the latter are connected to the LO modes, and the electronic calculations are relevant only to the acoustic and TO branches.

The situation is further complicated by the fact that it is only at the Brillouin-zone center that the electronic calculations do not include all the interactions of lattice and electric field. So the fitting procedure must reintroduce these interactions at small-momentum while leaving the dynamical matrices at other points unaffected.

To do this the Born effective charges are first calculated. These charges govern the LO-TO splitting. These charges must be zero for a nonpolar crystal.

Considering two ions in the basis  $\tau$  and  $\tau'$  at sites separated by lattice vector  $\mathbf{R}$ , the contribution to the inter-atomic force constants from the screened electrostatic energy between the two is

$$C_{\tau\tau'ii'}^{Coul}(\mathbf{R}) = \frac{\partial^2 E^{Coul}(\mathbf{R})}{\partial u_{\tau i} \partial u_{\tau' i'}}.$$

The derivatives are with respect to displacements from equilibrium along the corresponding ionic coordinates. (In this context it is appropriate to consider the screening appropriate to bulk conditions, since when all manipulations are completed, the only information retained is that relevant to the limit of small wave vector.) Gonze and Lee [30] write the reciprocal space transform, in accord with the Ewald [29] formulation by first defining

$$\begin{aligned} \widetilde{C}_{\tau\tau'ii'}^{Coul}(\mathbf{k}) &= \sum_{\mathbf{K}} \frac{4\pi}{\Omega} \frac{K_i K_{i'}}{\widetilde{K}^2} \exp(i\mathbf{K} \cdot (\mathbf{r}_\tau - \mathbf{r}_{\tau'})) \exp\left(\frac{-\widetilde{K}^2}{4\Lambda^2}\right) - \\ &\quad \sum_{\mathbf{R}} \Lambda^3 e^{i\mathbf{k} \cdot \mathbf{R}} H_{ii'}(\Lambda \Delta_{\tau\tau'}, \Lambda D_{\tau\tau'}) (\det \epsilon_\infty)^{-\frac{1}{2}} - \\ &\quad \frac{4}{3\sqrt{\pi}} \Lambda^3 \delta_{\tau\tau'} \epsilon_{\infty ii'}^{-1} (\det \epsilon_\infty)^{-\frac{1}{2}}. \end{aligned} \quad (4.16)$$

The reciprocal-space summation index has

$$\mathbf{K} = \mathbf{G} + \mathbf{k},$$

where  $\mathbf{G}$  runs over reciprocal-lattice vectors. The dielectric tensor  $\epsilon_\infty$  appears as a metric in reciprocal space, giving the definition,

$$\widetilde{K}^2 = \sum_{ii'} \epsilon_{ii'\infty} K_i K_{i'}.$$

The parameter  $\Lambda$  arises through the Ewald summation and is in general arbitrary and chosen for optimal convergence of the two sums. Eq. 4.16 uses the following three definitions:

$$H_{ii'}(\mathbf{x}, y) = \frac{x_i x_{i'}}{y^2} \left( \frac{3}{y^3} \operatorname{erfc}(y) + \frac{2}{\sqrt{\pi}} e^{-y^2} \left( \frac{3}{y^2} + 2 \right) \right) - \epsilon_{ii'\infty}^{-1} \left( \frac{\operatorname{erfc}(y)}{y^3} + \frac{2}{\sqrt{\pi}} \frac{e^{-y^2}}{y^2} \right),$$

$$\Delta_{\tau\tau'i} = \sum_{i'} \epsilon_{ii'\infty} (R_{i'} + s_{\tau i'} - s_{\tau' i'}),$$

and

$$D_{\tau\tau'} = \sqrt{\Delta_{\tau\tau'} \cdot (\mathbf{s}_\tau - \mathbf{s}_{\tau'})}.$$



It is now possible to write

$$\tilde{\mathbf{C}}^{Coul}(\mathbf{k}) = \frac{1}{N} \sum_{\mathbf{R}} \mathbf{C}^{Coul}(\mathbf{R}) e^{-i\mathbf{k}\cdot\mathbf{R}} \quad (4.17)$$

as

$$\tilde{C}_{\tau\tau'ii'}^{Coul}(\mathbf{k}) = \sum_{jj'} Z_{ji}^{\tau} Z_{j'i'}^{\tau'} \overline{C}_{\tau\tau'ii'}^{Coul}(\mathbf{k}) - \delta_{\tau\tau'} \sum_{\tau''} \sum_{jj'} Z_{ji}^{\tau} Z_{j'i'}^{\tau''} \overline{C}_{\tau\tau''ii'}^{Coul}(\mathbf{k} = 0). \quad (4.18)$$

The real space sum in Eq. 4.16 has a well-defined limit as  $\mathbf{k}$  tends to zero, although for  $\tau = \tau'$ , the  $\mathbf{R} = 0$  term is divergent and precisely negated by an identical contribution from the second term on the right-hand side of Equation 4.18. In the limit of small  $\mathbf{k}$ , the nonanalytic, directionally dependent term  $(4\pi/\Omega)k_i k_j / \widetilde{k}^2$ , arising from the  $\mathbf{G} = 0$  term in the reciprocal space sum of Equation 4.16, accounts entirely for the macroscopic fields and LO-TO repulsion. Since the relation

$$\sum_{\tau} Z_{ii'}^{\tau} = 0 \quad (4.19)$$

holds,  $\overline{C}_{\tau\tau''ii'}^{Coul}(\mathbf{k} = 0)$  in Equation 4.18 can be replaced by its analytical part.

As mentioned, the small- $\mathbf{k}$ , nonanalytic contribution to  $\tilde{\mathbf{C}}(\mathbf{k})$  is missing in a supercell calculation. In order to reintroduce it, let the tensor  $\tilde{\mathbf{C}}^{DFT}(\mathbf{k})$  indicate the Born-von Karman force constants calculated within the framework of the above discussion, and hence missing the contribution of macroscopic fields. The transformation between the Born-von Karman and interatomic forces constants can be modified as:

$$\tilde{\mathbf{C}}^{DFT}(\mathbf{k}) - \mathbf{T}(\mathbf{k}) = \frac{1}{N} \sum_{\mathbf{R}} e^{-i\mathbf{k}\cdot\mathbf{R}} \hat{\mathbf{C}}(\mathbf{R}) \quad (4.20)$$

with the notation,

$$\begin{aligned} \mathbf{T}(\mathbf{k}) &= \tilde{\mathbf{C}}^{an}(\mathbf{k}) : \mathbf{k} = 0 \\ \mathbf{T}(\mathbf{k}) &= \tilde{\mathbf{C}}^{Coul}(\mathbf{k}) : \mathbf{k} \neq 0, \end{aligned} \quad (4.21)$$

and  $\tilde{\mathbf{C}}^{an}(\mathbf{k})$  is the analytical part of  $\tilde{\mathbf{C}}^{Coul}(\mathbf{k})$ . Within the fitting procedure, the Born-von Karman and inter-atomic force constants are now replaced by  $\hat{\mathbf{C}}(\mathbf{R})$ , and  $\tilde{\mathbf{C}}^{DFT}(\mathbf{k}) - \mathbf{T}(\mathbf{k})$ , respectively.

Then, the full Born-von Karman force tensor, with the effects of the macroscopic fields, is:

$$\tilde{\mathbf{C}}(\mathbf{k}) = \tilde{\mathbf{C}}^{Coul}(\mathbf{k}) + \frac{1}{N} \sum_{\mathbf{R}} e^{-i\mathbf{k}\cdot\mathbf{R}} \hat{\mathbf{C}}(\mathbf{R}). \quad (4.22)$$

#### 4.4 Results for GaAs and GaP

Phonon dispersion curves and densities of states for GaAs and GaP are presented in Figures 1-4. The wave-vector sampling corresponds to that listed for the Si and Ge calculations of the preceding section. For GaAs, all ion-pair interactions are included for a cutoff separation of  $15 a_0$ , and the calculated lattice constant is  $10.46 a_0$ , and for GaP, the cutoff distance is  $15.5 a_0$ , and the lattice constant is  $10.09 a_0$ .

In zincblende systems, the Born-effective-charge tensor is cubic and diagonal, and so the Born effective charge of any basis ion can be written as a scalar,  $Z_\tau$ . In these systems, the change in the polarization with respect to crystal translation must be zero. Since any  $\mathbf{k} = 0$  strain of the crystal can be generated with a crystal translation and a change in the relative coordinate of the two basis ions, the change in the polarization for such a strain can only depend on the change in the relative basis coordinate. The adiabatic displacement can be considered to take place with ion  $\tau$  at rest and ion  $\tau'$  displaced by  $x_i$ , or with ion  $\tau'$  at rest and ion  $\tau$  displaced by  $-x_i$ , and the polarization change must be the same in either case. The charge neutrality condition of Eq. 4.19 follows. The calculated charge associated with the gallium ion in GaP is  $2.17e$ , and  $2.12e$  in GaAs. The phosphorus and arsenic ions, respectively, provide the canceling charge.

A comparison of the two dispersion plots is interesting. For GaAs, the near crossing of the  $TO(\mathbf{\Gamma})$  and  $LA(\mathbf{X})$  modes is observed. In diamond-type materials, the degeneracy is

symmetry-enforced. By contrast, in GaP, there is no such near degeneracy. This result may be motivated by noting that in the Einstein approximation to the optical vibrations, each ion vibrates independently, and there is no dispersion in the optical phonon frequencies. In diamond-type crystals, the Einstein approximation does not hold, to the extent that the optical frequencies bend downward approaching the Brillouin zone boundary, so that the condition,  $\omega_{TO(\Gamma)} = \omega_{LA(\mathbf{x})}$  is met. It may be expected that the Einstein approximation is better realized in crystals where the basis ions have significant mass mismatch, and hence the equivalent status of basis ions in diamond-type structures is greatly violated. In such materials, a clear gap may be anticipated between the longitudinal and optical acoustic phonon branches. This is indeed seen in the dispersion calculation of GaP.

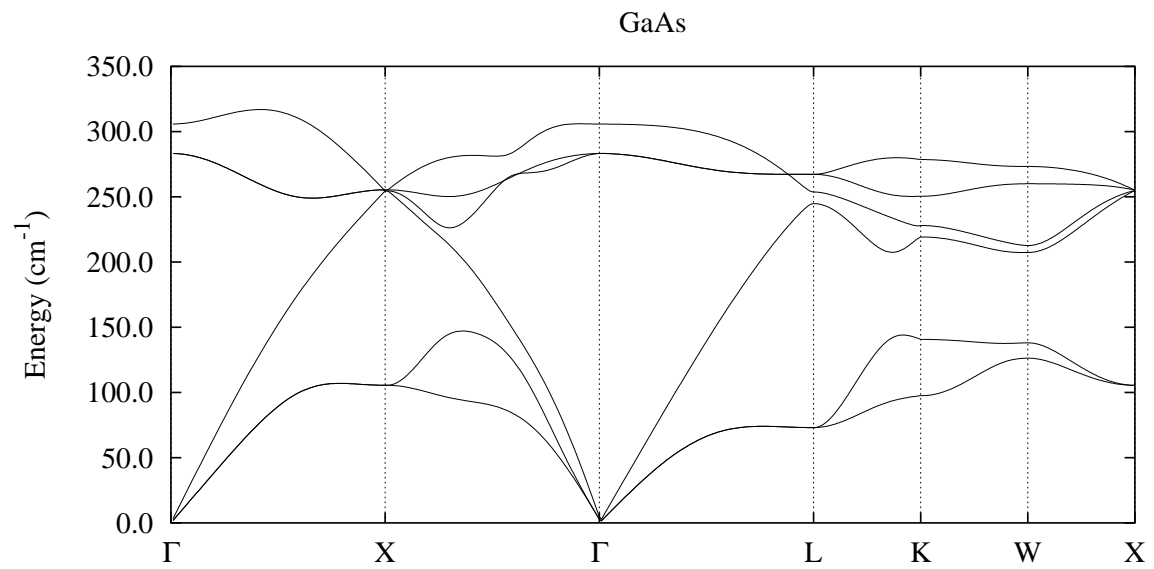


Figure 4.1: Calculated phonon dispersion in GaAs.

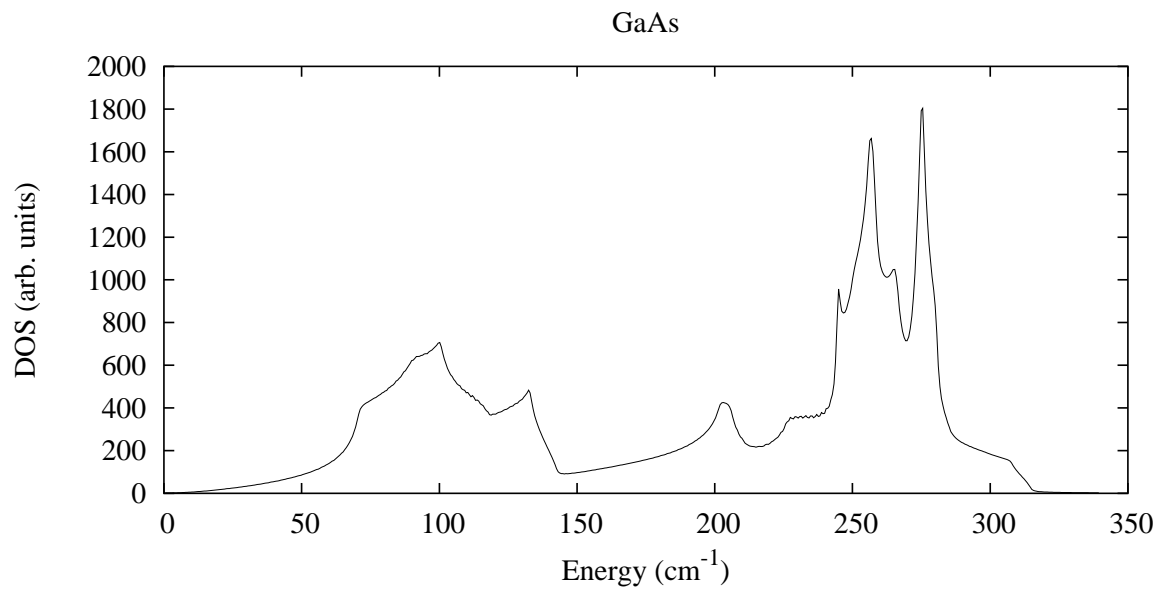


Figure 4.2: Calculated phonon density of states in GaAs.

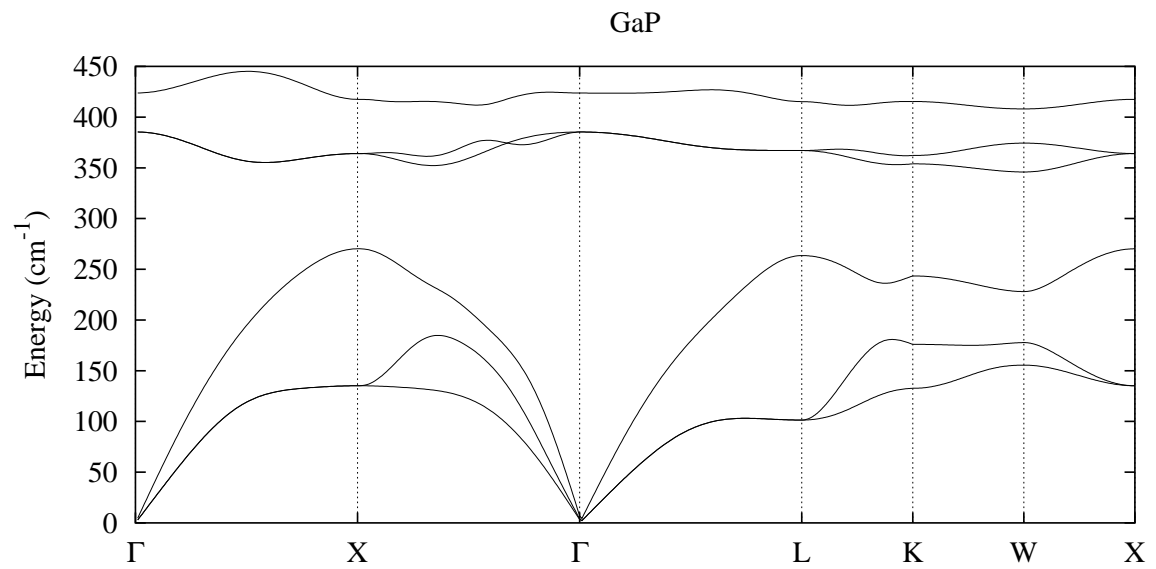


Figure 4.3: Calculated phonon dispersion in GaP.

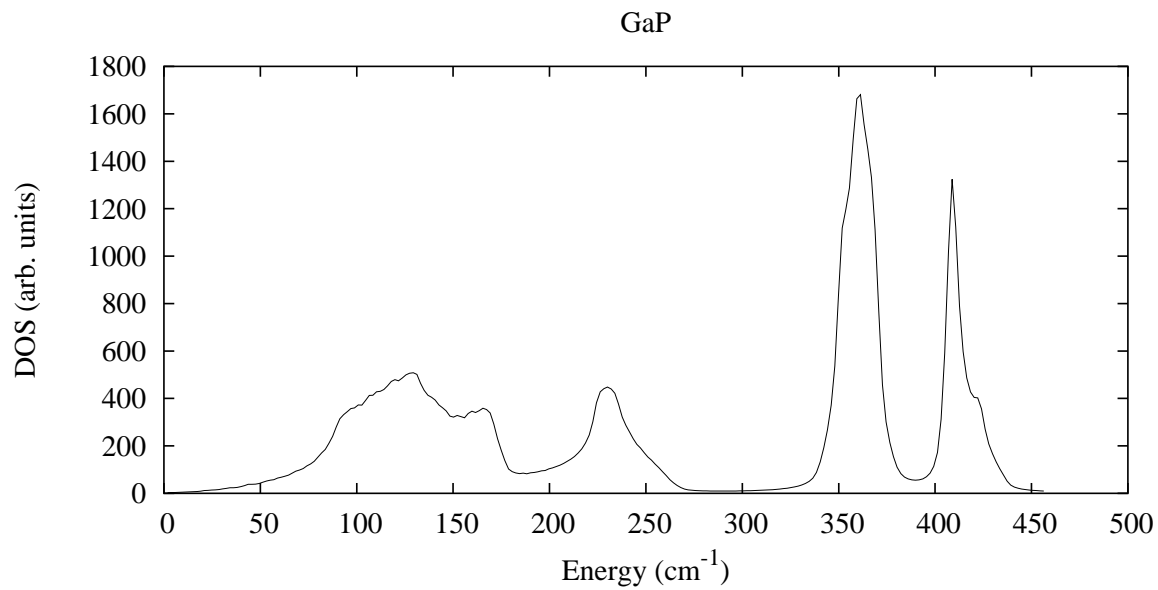


Figure 4.4: Calculated phonon density of states in GaP.

## Chapter 5

### Calculation of Anharmonic Effects

#### 5.1 Beyond the Harmonic Approximation

Within the harmonic approximation, the phonon dispersion expresses the complete characterization of the vibrational spectrum of a crystal. Experiments, such as neutron and x-ray scattering, and the zero-parameter calculations of detailed spectra, demonstrate that the harmonic approximation is quite appropriate, in that the phonons constitute a well-defined excitation spectrum in typical materials.

The crystal's state, in the harmonic approximation, is a superposition of many-body states, with a particular many-body wave function written,

$$\Psi(\{\alpha_{n\mathbf{k}\nu}\}) = \prod_{\mathbf{k}\nu} \phi_{\mathbf{k}\nu}(\alpha_{n\mathbf{k}\nu}, q_{\mathbf{k}\nu}), \quad (5.1)$$

where the modes states  $\phi_{\mathbf{k}\nu}$ , and normal coordinates,  $q_{\mathbf{k}\nu}$ , are indexed by wave vector and phonon branch. The modes can be considered as a set of independent harmonic oscillators.

The state of each mode is

$$\phi_{\mathbf{k}\nu}(\alpha_{n\mathbf{k}\nu}, q_{\mathbf{k}\nu}) = \sum_n \alpha_{n\mathbf{k}\nu} (a_{\mathbf{k}\nu}^{\dagger})^n \phi_{\mathbf{k}\nu}^0(q_{\mathbf{k}\nu}), \quad (5.2)$$

the general harmonic oscillator states being written as arbitrary superpositions, with amplitudes  $\alpha_{n\mathbf{k}\nu}$ , of states formed through  $n$  creation operations on the ground state:

$$\phi_{\mathbf{k}\nu}^0(q_{\mathbf{k}\nu}) = \left(\frac{\omega_{\mathbf{k}\nu}^2}{\pi}\right)^{1/4} e^{-\frac{1}{2}q_{\mathbf{k}\nu}^2 \omega_{\mathbf{k}\nu}^2}. \quad (5.3)$$

A general many-body state may then be formed from superpositions of the above many body states,

$$\Psi = \sum_{\{\alpha_{n\mathbf{k}\nu}\}} A_{\{\alpha_{n\mathbf{k}\nu}\}} \Psi(\{\alpha_{n\mathbf{k}\nu}\}). \quad (5.4)$$



The eigenvalues of the dynamical matrix are  $\omega_{\mathbf{k}\nu}^2$ , with normalized eigenvectors  $\mathbf{v}_{\mathbf{k}\nu}$ .

Nevertheless, anharmonic terms—which are cubic or higher order in ionic displacements from equilibrium—must be present in the Born-Oppenheimer potential energy. In the absence of such terms, the harmonic approximation allows unitary transformations which decouple the equations of motion. But in the presence of anharmonic terms, there is energy transfer among modes. If these terms are weak compared to the harmonic forces, an expected result is the damping—or acquisition of a finite lifetime—of the phonons, which nonetheless possess well-defined resonance frequencies. These lifetimes, in accord with the uncertainty principle, can be spectroscopically measured through the linewidth of the resonances. Such experiments have been widely carried out, particularly measurement of zero-momentum phonon linewidths with inelastic light, or Raman, scattering.

Of particular interest here is in the lifetime of the zero-momentum, optical phonon in diamond-type crystals, or an excitation of the mode  $\Psi_{\Gamma}$ , the subscript standing in for any of the three symmetry-equivalent, long-wavelength optical branches. The finite lifetime arising from *cubic* anharmonic terms in the Born-Oppenheimer potential will be considered. While the anharmonic terms are not limited to those cubic in ionic displacements, the retention of cubic terms alone is a natural beginning for a theoretical evaluation of the damping. Accordingly, the anharmonic Hamiltonian to be considered here is:

$$\begin{aligned} H_{anh} &= \frac{1}{6} \sum_{\mathbf{R}\mathbf{R}'\mathbf{R}''} \sum_{\tau\tau'\tau''} \sum_{ii'i''} U_{ii'i''}^{B-O}(\mathbf{R}\tau, \mathbf{R}'\tau', \mathbf{R}''\tau'') x_{i\tau}(\mathbf{R}) x_{i'\tau'}(\mathbf{R}') x_{i''\tau''}(\mathbf{R}'') \\ &= \frac{1}{6\sqrt{N}} \sum_{\mathbf{k}\nu\mathbf{k}'\nu'\mathbf{k}''\nu''} \delta(\mathbf{k} + \mathbf{k}' + \mathbf{k}'') \Phi(\mathbf{k}\nu, \mathbf{k}'\nu', \mathbf{k}''\nu'') q_{\mathbf{k}\nu} q_{\mathbf{k}'\nu'} q_{\mathbf{k}''\nu''}. \end{aligned} \quad (5.5)$$

The Bloch-representation cubic terms above are related to the cubic coefficients of the ionic coordinates according to:

$$\begin{aligned} \Phi(\mathbf{k}\nu, \mathbf{k}'\nu', \mathbf{k}''\nu'') &= \\ & \sum_{\mathbf{R}'\mathbf{R}''} \sum_{\tau'\tau''} \sum_{ii'i''} \frac{U_{ii'i''}^{B-O}(0\tau, \mathbf{R}'\tau', \mathbf{R}''\tau'')}{\sqrt{m_{\tau}m_{\tau'}m_{\tau''}}} v_{\mathbf{k}\nu\tau i} v_{\mathbf{k}'\nu'\tau' i'} v_{\mathbf{k}''\nu''\tau'' i''} e^{i(\mathbf{k}'\cdot\mathbf{R}'+\mathbf{k}''\cdot\mathbf{R}'')}. \end{aligned} \quad (5.6)$$

The the full cubic Hamiltonian can be written in this form as a consequence of invariance with lattice-vector translation.

For the following derivations, the phonon normal coordinates are best expressed in terms of the phonon creation and destruction operators:

$$q_{\mathbf{k}\nu} = \sqrt{\frac{\hbar}{2\omega_{\mathbf{k}\nu}}}(a_{\mathbf{k}\nu} + a_{-\mathbf{k}\nu}^{\dagger}). \quad (5.7)$$

## 5.2 Long-wave Optical Phonon Lifetime

Inspection of the state corresponding to a single excitation of the long-wave phonon,  $\Psi_{\Gamma} = a_{\Gamma}^{\dagger}\Psi_0$ , where the many-body ground state is indicated on the right, leads to identification of the states which are relevant to the lifetime of  $\Psi_{\Gamma}$ . The matrix elements of  $H_{anh}$  between  $\Psi_{\Gamma}$  and any final state are nonzero only if the final state is formed from the many-body ground by the action of two or four phonon creation operators. This is seen by recognizing that when the matrix elements are written in terms of the many-body ground state, the operator products which appear must contain an even number of phonon coordinates in order for the phonon creation and annihilation operators to be paired off. For the matrix elements between  $\Psi_{\Gamma}$  and any final state to be non-zero, energy and momentum conservation must hold, further restricting the relevant final states to those which are two-phonon, or those which can be formed from the many-body ground state with a product of two creation operators. Momentum conservation also ensures that the final states correspond to two-phonon states where the two are of equal and opposite wave vector. Here these states are denoted  $\Psi_{\mathbf{k}\nu-\mathbf{k}\nu'}$

As a result, Eq. 5.5 can, for the purposes of calculating the lifetime of  $\Psi_{\Gamma}$ , be reduced to:

$$H_{anh} = \frac{1}{2\sqrt{N}} \sum_{\mathbf{k}\nu\nu'} \Phi(\mathbf{k}\nu, -\mathbf{k}\nu', \Gamma) q_{\mathbf{k}\nu} q_{-\mathbf{k}\nu'} q_{\Gamma}. \quad (5.8)$$

A periodic displacement configuration, as represented by a phonon normal coordinate,

for instance, can be expressed as  $\mathbf{x}_\tau(\mathbf{R}) = \mathbf{d}_\tau e^{i(\mathbf{k}\cdot\mathbf{R})}$ . For  $\mathbf{k} = 0$ , any such configuration can be generated by a relative sublattice displacement together with some crystal translation. Because of invariance with respect to translation of the entire crystal, then, the cubic coefficient in the potential energy can be rewritten:

$$\frac{\partial^3 U}{\partial q_\Gamma \partial q_{\mathbf{k}\nu} \partial q_{-\mathbf{k}\nu'}} = \frac{1}{\sqrt{N}\mu} \frac{\partial^3 U}{\partial u \partial q_{\mathbf{k}\nu} \partial q_{-\mathbf{k}\nu'}} = \frac{1}{2\sqrt{N}\mu} \sum_{\tau\tau'ii'} \frac{\partial D_{ii'}^{\tau\tau'}(\mathbf{k})}{\partial u} v_{\mathbf{k}\nu\tau i} v_{-\mathbf{k}\nu'\tau' i'}, \quad (5.9)$$

where  $u$  is the magnitude of the change in sublattice relative coordinate, evaluated about equilibrium, and  $\mu$  is the reduced mass of the basis ions. The relation,

$$\frac{\partial^3 U}{\partial q_\Gamma \partial q_{\mathbf{k}\nu} \partial q_{-\mathbf{k}\nu'}} = \frac{1}{\sqrt{N}} \Phi(\mathbf{k}\nu, -\mathbf{k}\nu', \Gamma), \quad (5.10)$$

should also be noted.

The inverse of the long-wave phonon lifetime  $2\gamma$ , then, can be calculated with the following expression:

$$\begin{aligned} 2\gamma = & \quad (5.11) \\ & \frac{2\pi}{\hbar^2} \frac{1}{2} \sum_{\mathbf{Q}\lambda\lambda'} \left| \sum_{\mathbf{k}\nu\nu'} \langle \Psi_\Gamma | H_{anh} | \Psi_{\mathbf{Q}\lambda-\mathbf{Q}\lambda'} \rangle \right|^2 \delta(\omega_\Gamma - \omega_{\mathbf{Q}\lambda} - \omega_{-\mathbf{Q}\lambda'}) = \\ & \frac{\pi\hbar}{8\mu\omega_\Gamma N} \sum_{\mathbf{Q}\lambda\lambda'} \left| \sum_{\mathbf{k}\nu\nu'} \frac{(\delta_{\mathbf{k},\mathbf{Q}} \delta_{\nu,\lambda} \delta_{\nu',\lambda'} + \delta_{-\mathbf{k},\mathbf{Q}} \delta_{\nu,\lambda'} \delta_{\nu',\lambda})}{2\sqrt{\omega_{\mathbf{k}\nu} \omega_{-\mathbf{k}\nu'}}} M_{\nu\nu'\mathbf{k}} \right|^2 \delta(\omega_\Gamma - \omega_{\mathbf{Q}\lambda} - \omega_{-\mathbf{Q}\lambda'}) \\ & = \frac{\pi\hbar}{8\mu\omega_\Gamma N} \sum_{\mathbf{k}\nu\nu'} \frac{1}{\omega_{\mathbf{k}\nu} \omega_{-\mathbf{k}\nu'}} |M_{\nu\nu'\mathbf{k}}|^2 \delta(\omega_\Gamma - \omega_{\mathbf{k}\nu} - \omega_{-\mathbf{k}\nu'}), \end{aligned}$$

with the definition,

$$M_{\nu\nu'\mathbf{k}} = \sum_{\tau\tau'ii'} \frac{\partial D_{ii'}^{\tau\tau'}(\mathbf{k})}{\partial u} v_{\mathbf{k}\nu\tau i} v_{-\mathbf{k}\nu'\tau' i'}. \quad (5.12)$$

The above is derived by application of Fermi's Golden Rule, where the matrix elements of the operator in Eq. 5.8 are evaluated between  $\Psi_\Gamma$  and the full phonon Fock space, subject to the above discussed restrictions. The expression in Eq. 5.12 is appropriate to a system at zero temperature.

Because the anharmonic lifetime effects can be modeled with a small imaginary part to the phonon energy, corresponding to  $\gamma$ , the calculations can be compared with experimental

probes where the spectroscopic response is fit to Lorentzian parameters.

### 5.3 The Sublattice Displacement and Symmetry Considerations

The lifetime  $2\gamma$  can be evaluated by calculating the change in the dynamical matrix, throughout the Brillouin zone, with respect to a sublattice shift, as can be seen in Eq. 5.9. In diamond-type crystals, the restoring forces resulting from a sublattice shift are isotropic with respect to the shift's direction. Consistent with the notation in preceding sections, then, the cubic term in Eq. 5.12 is evaluated by calculating the full phonon dispersion for sublattice shifts along positive and negative projections along a Cartesian direction, and taking the finite difference. The phonon frequencies appearing in the lifetime expression are evaluated for no sublattice shift. The magnitude of each displacement is  $0.1 a_0$ . All terms are included in the finite difference, including the long-range Coulomb interaction appearing in the Ewald-Kornfeld sums, which are evaluated for each distortion.

The dynamical matrices for two distorted crystals—one with a positive and one with a negative sublattice shift—are subtracted to evaluate the derivative of the dynamical matrix throughout the Brillouin zone. This necessitates repeating the symmetry analysis for the distorted crystals. These possess symmetry operations which comprise a smaller subset of the undistorted crystal's symmetry group. Thus, evaluation of the dynamical matrix at the same set of wave vectors for the distorted and undistorted crystals gives less information for the distorted than the undistorted crystal. In order to retain equivalent physical sampling for each case, then, the wave-vector sampling is increased for the distorted crystal. For the distorted case, the original set of wave vectors is supplemented by those which fold to the original set under the full symmetry group, but not under the reduced group. For the distorted crystal then, the equivalent set of wave vectors correspond to an expanded set of independent Born-von Karman force constants, which corresponds to an expanded set of parameters entering the inter-atomic force constants within the interaction range. The

interaction length range is taken to be the same for the distorted and undistorted lattice, so as to retain the same physical set of interactions.

## 5.4 Results and Uncertainty

For Si, this calculation gives the result  $2\gamma = 2 \text{ cm}^{-1}$ , and for Ge and diamond, respectively,  $0.6 \text{ cm}^{-1}$ , and  $3 \text{ cm}^{-1}$ . These results, being evaluated with Eq. 5.12, are appropriate to the zero-temperature limit. The corresponding experimental values range from  $1.2$  to  $2.8 \text{ cm}^{-1}$  for Si,  $0.75$  to  $1.4 \text{ cm}^{-1}$  for Ge, and  $1.2$  to  $2.9 \text{ cm}^{-1}$  for diamond [31]. The results of prior first-principles calculations are  $1.48$  and  $1.44 \text{ cm}^{-1}$  for Si,  $1.01$  and  $0.97 \text{ cm}^{-1}$  for diamond, and  $0.67 \text{ cm}^{-1}$  for Ge [32].

Evaluating Eq. 5.12 with a Brillouin zone sampling set of 64,000 points, the lifetime for Si is converged to within 1 % for Lorentzian simulations of the Dirac function with widths of  $0.3 \text{ cm}^{-1}$ ,  $0.1 \text{ cm}^{-1}$ , and  $0.03 \text{ cm}^{-1}$ . Using the same widths, increasing the Brillouin zone sampling to 512,000 points improves the convergence with respect to Lorentzian parameters to less than 1 %, and the result is converged to that of the more limited Brillouin zone sampling to within 5 %. Very similar convergence behavior is seen in Ge and diamond, so that for each material, numerical uncertainty associated with broadening and sampling is 5 %.

The remaining uncertainties in the reported values are associated with the computed dynamical matrix elements—and the consequent phonon frequencies—and evaluation of their change with sublattice displacement.

The sensitivity of Eq. 5.12 to the optical phonon frequencies comes from the two-phonon kinematics, as expressed in the appearance of  $\omega_{\Gamma}$  in the argument of the Dirac function. Changing the value of  $\omega_{\Gamma}$  in Eq. 5.12 by 10 % modifies the lifetimes by approximately 30 %.

Inspection of the phonon dispersions clearly indicates that energy conservation, again

expressed through the Dirac function of Eq. 5.12, that the dominant two-phonon decay channels are acoustic modes. The sensitivity of the lifetime to these modes comes through their frequencies and changes in appropriate projections of the dynamical matrix. The variation in the relevant frequencies with sublattice shift is greater than the uncertainty in the frequencies themselves, estimated at  $\leq 20\%$ . The uncertainty in appropriate projections of the dynamical matrix is then the dominant uncertainty, contributing a 40 % uncertainty to the lifetime.

In light of the above analyses, the lifetimes reported here should be considered determined within a factor of 2.

## Chapter 6

### Anharmonic Effects and Infrared Response

#### 6.1 Phonons and Infrared Absorption

The harmonic approximation is insufficient for a close inspection of the frequency dependence of the dielectric response in the infrared. For instance, in the absence of direct multiphonon transitions, the harmonic approximation predicts infinitely sharp absorption at  $\omega_{TO}$ , the frequency of the long-wavelength, transverse optical phonon, or the dispersion oscillator, and nowhere else [4]. Measured spectra, however, show finite linewidth and asymmetric lineshape of the infrared-active phonon and very broad background absorption, which can exhibit fine features and singularities [33, 34, 35, 36], and temperature-dependent absorption in the far-infrared [37]. These effects are closely related to the lifetime effects on Raman spectra previously discussed.

A theory which incorporates the phonon-phonon interaction into the theory of the optical response, where anharmonic terms in a crystal's interionic potential introduce interaction among the phonons, can help to explain asymmetric broadening and background absorption [6]. As an example, in the long-wavelength limit, an infrared photon can, through a virtual excitation of the infrared-active phonon and anharmonic corrections to its quantum state, be absorbed by a pair of phonons whose momenta sum to nearly zero (relative to Brillouin zone dimensions) and whose energies sum to that of the photon. These sum processes endow the spectra with rich structure. At nonzero temperatures, the onset of difference processes, where one phonon is emitted and another is absorbed along with the photon, give a strong temperature dependence to the far-infrared absorption.

First-principles consideration of the phonon-phonon interaction, which determines the

spectral structure of the response, and the phonon-photon interaction, which determines the overall oscillator strength, are key to this work. Realistic, observable quantities arising from phonon-phonon interactions, or anharmonic effects, are now calculated as well as measured, such as the linewidth, asymmetric shape and temperature dependence of Raman modes [32, 38, 39, 40, 41]. The present theoretical work on zero-temperature, Raman mode lifetimes has been discussed. The treatment of anharmonic effects on the optical response closely follows the theoretical studies of Raman spectra, but with a study of their role in the dielectric function.

Phonon-induced dipoles, representing the phonon-photon interaction, are given by the Born effective charges. These charges enhance the longitudinal optical phonon frequency while coupling the transverse optical phonon to infrared photons, and are calculated according to the modern theory of polarization [7], as discussed. With these charges and the infrared-active phonon's self-energy, the spectral profile and the oscillator strength can be calculated, and all the optical constants can be obtained.

The degree of similarity between observed spectra and the calculations reported here strongly indicates that modern first-principles calculations and perturbative formalism reflect the microscopic processes governing infrared optical response, and may serve to stimulate further work toward detailed characterization of crystalline materials.

Figure 6.1 summarizes these results and their comparison with measured spectra. Its examination suggests that two-phonon processes are present over the entire infrared spectral range through  $2\omega_{TO}$ . Below  $\omega_{TO}$ , we predict the measured low-energy absorption tail well into the far-infrared spectrum, and the expected temperature dependence [37]. The lineshape of the infrared-active phonon is strikingly reproduced. Between  $\omega_{TO}$  and  $2\omega_{TO}$ , absorption and transparency features demonstrate a convincing correspondence with measured data. These are associated, respectively, with critical points and gaps in the zero-momentum, two-phonon density of states. There is more structure to the two-phonon



spectrum of GaP than of GaAs, including a prominent narrow band of suppressed absorption, because its larger ionic mass mismatch widens the energy difference between various phonon branches. The data for GaAs are from Ref. [35] and references therein. Some data points are from fits to an oscillator model, and are “generally not determined better than  $\pm 30\%$ ” [35]. The reststrahlen and low-frequency data for GaP are from Ref. [34] and references therein. The low-temperature and room-temperature data points above the reststrahlen are from Ref. [33], and the data are from transmission measurements on a high-purity sample.

In Figure 6.1, the optical response is characterized with the absorption coefficient,  $\alpha(\nu) = 4\pi\nu k(\nu)$ , where  $k(\nu)$  is the index of absorption, and  $\nu$  is photon energy in  $\text{cm}^{-1}$ .

The strong temperature dependence of the absorption in the far infrared is highlighted in Figures 6.2 and 6.3. The experimental and theoretical results are plotted at 10-300 K for comparison.

Below, the role of phonons in the dielectric response is summarized, the anharmonic contributions and their many-body treatment are discussed, and finally results and details of the calculations are presented.

## 6.2 Dielectric Response of the Lattice

In GaAs and GaP, infrared optical properties are dominated by phonons. The Hamiltonian density for a polar crystal in the presence of an electric field,  $\mathbf{E}$ , can be written as

$$H = \sum_{\lambda} \frac{1}{2N\Omega} (\omega_{\lambda}^2 q_{\lambda}^2 + \dot{q}_{\lambda}^2) + \mathbf{E} \cdot \mathbf{P}^{mac} + H_{anh} + H_{mp}, \quad (6.1)$$

where  $q_{\lambda}$  and  $\omega_{\lambda}$  are the normal coordinate and frequency, respectively, of a phonon with wave vector and branch indexed by  $\lambda$ . The unit-cell volume is  $\Omega$  and the number of Bravais-lattice sites is  $N$ . The dimensions of the quantity  $\mathbf{P}^{mac}$  are dipole moment per unit volume.

Anharmonic potential-energy terms are assumed to be small, and expressed with  $H_{anh}$ . Direct dipole transitions to multiphonon states are represented with  $H_{mp}$ . This coupling has been observed and calculated [42, 43], but is not accounted for here.

The macroscopic polarization in Eq. 6.1 can be written as,

$$P_i^{mac} = \frac{1}{\Omega} \sum_{\nu=TO} \sum_{\tau j} \frac{1}{\sqrt{m_\tau}} Z_{ij}^\tau q_\nu \epsilon_{\tau j}^\nu. \quad (6.2)$$

In the above,  $m_\tau$  is the mass of ion  $\tau$ , the phonon normal coordinate index,  $\nu$ , runs strictly over the infrared-active phonons, and  $\epsilon_{\tau j}^\nu$  is a component of the polarization of such a phonon. Cartesian directions are indicated with the indices  $i$  and  $j$ . The charges are expressed as the change in macroscopic polarization with respect to sublattice displacement:

$$Z_{ij}^\tau = \Omega \frac{\partial P_i^{mac}}{\partial u_{\tau j}}. \quad (6.3)$$

Formally, the following expressions can be derived with a Green's function formalism [44]. A heuristic oscillator model for the response can be written by expressing the effects of  $H_{anh}$  as a complex damping term, or self-energy that modifies  $\omega_{TO}$ :  $\Sigma_{TO}(\omega) = \Delta(\omega) - i\gamma(\omega)$ . Substituting Eq. 6.2 into Eq. 6.1, solving the driven-oscillator equation of motion for an infrared-active phonon's normal coordinate, and then taking the sum indicated in Eq. 6.2, the polarization is found to be:

$$P_i^{mac}(\omega) = \frac{1}{\Omega} \sum_{\tau\tau' i' j j'} \sum_{\nu=TO} \frac{Z_{ij}^\tau Z_{i'j'}^{\tau'} \epsilon_{\tau j}^\nu \epsilon_{\tau' j'}^{\nu'} E_{i'}(\omega)}{2\sqrt{m_\tau m_{\tau'}} \omega_{TO}} \left( \frac{1}{\omega + \omega_{TO} + \Sigma_{TO}(\omega)} - \frac{1}{\omega - \omega_{TO} - \Sigma_{TO}(\omega)} \right). \quad (6.4)$$

The dielectric function follows immediately. It is written [28],

$$\epsilon_{ii'}(\omega) = \epsilon_{\infty ii'} + \frac{4\pi}{\Omega} \sum_{\tau\tau' i' j j'} \sum_{\nu=TO} \frac{Z_{ij}^\tau Z_{i'j'}^{\tau'} \epsilon_{\tau j}^\nu \epsilon_{\tau' j'}^{\nu'}}{2\sqrt{m_\tau m_{\tau'}} \omega_{TO}} \left( \frac{1}{\omega + \omega_{TO} + \Sigma_{TO}(\omega)} - \frac{1}{\omega - \omega_{TO} - \Sigma_{TO}(\omega)} \right) \quad (6.5)$$

with  $\epsilon_{\infty ii'}$  representing the high-frequency dielectric constant. When all the infrared-active

modes are symmetry-related, as is the case in a zincblende system, their frequencies and self-energies are equal, and denoted by the subscript  $TO$  above.

### 6.3 The Phonon Self-Energy

Low-temperature phonon-phonon interactions have been the subject of thorough field-theoretic analyses [5, 6, 45, 46]. Modern implementations successfully calculate realistic thermodynamic and spectral properties which originate from such interactions [47, 48], demonstrating the valuable predictive nature of first-principles studies. Phonon-phonon scattering events are ranked with a dimensionless expansion parameter, for which Van Hove et al have posited the ratio of zero-point ion delocalization to nearest-neighbor lengths [49]. The theory establishes lowest-order contributions to the anharmonic self-energy of a long-wave phonon from three distinct multiphonon processes [5, 46]. These are shown in Figure 6.4. One of these processes, (a), involves a single vertex, making it first order in  $H_{anh}$ , but second-order in the expansion parameter because the vertex involves a four-phonon interaction. The remaining two processes, (b) and (c), each involve three-phonon vertices, which are first-order in the expansion parameter, and are second-order in  $H_{anh}$ , because of the appearance of two vertices in the diagrams. Hence each of the three processes is second-order in the expansion parameter, according to the theory.

The four-phonon process and one of the three-phonon processes represent simultaneous absorption and reemission of a phonon by the infrared-active phonon. Such interactions are instantaneous, and therefore independent of frequency, contributing exclusively a line shift [50]. The interest of this work is in spectral structure and multiphonon processes, so frequency-independent terms are neglected. In any case, the calculations assume the theoretically relaxed rather than actual lattice constant, so the positions of  $\omega_{TO}$  and related spectral features are affected by other factors as well.

The remaining term, (c), reflects the infrared-active phonon's coupling to phonon-

pair states of opposite crystal momenta,  $\mathbf{k}$  and  $-\mathbf{k}$ , where their role has been compared to that of a “viscous medium” [4], and the matrix element between the infrared-active phonon and such a state is

$$M_{\nu\nu'\mathbf{k}} = \sum_{\tau\tau'ii'} \frac{\partial D_{ii'}^{\tau\tau'}(\mathbf{k})}{\partial u} v_{\tau i}^{\mathbf{k}\nu} v_{\tau' i'}^{-\mathbf{k}\nu'}. \quad (6.6)$$

The derivative of the dynamical matrix,  $D_{ii'}^{\tau\tau'}(\mathbf{k})$ , is taken with respect to the sublattice relative coordinate, as earlier discussed. For a zincblende crystal, the relevant anharmonic contribution to the Hamiltonian is:

$$H_{anh} = \frac{1}{2N\Omega\sqrt{N}\mu} \sum_{\nu=TO} \sum_{\mathbf{k}\alpha\beta} M_{\alpha\beta\mathbf{k}} q_{\mathbf{k}\alpha} q_{-\mathbf{k}\beta} q_{\nu}. \quad (6.7)$$

The prefactor includes the reduced mass,  $\mu = (m_{Ga}^{-1} + m_{As}^{-1})^{-1}$ , or  $\mu = (m_{Ga}^{-1} + m_P^{-1})^{-1}$ . The anharmonic interaction leads to a frequency- and temperature-dependent shift and damping of the infrared-active phonon, expressed as the self-energy,

$$\begin{aligned} \Sigma_{TO}(\omega) = & -\frac{\hbar}{16\mu\omega_{TO}} \frac{1}{N} \sum_{\mathbf{k}\nu\nu'} \frac{|M_{\nu\nu'\mathbf{k}}|^2}{\omega_{\mathbf{k}\nu}\omega_{-\mathbf{k}\nu'}} \\ & \left[ \left( \frac{1 + n_{\mathbf{k}\nu} + n_{-\mathbf{k}\nu'}}{\omega_{\mathbf{k}\nu} + \omega_{-\mathbf{k}\nu'} - \omega - i\eta} \right) + \right. \\ & \left( \frac{1 + n_{\mathbf{k}\nu} + n_{-\mathbf{k}\nu'}}{\omega_{\mathbf{k}\nu} + \omega_{-\mathbf{k}\nu'} + \omega + i\eta} \right) \\ & + \left( \frac{n_{\mathbf{k}\nu'} - n_{\mathbf{k}\nu}}{\omega_{\mathbf{k}\nu} - \omega_{\mathbf{k}\nu'} - \omega - i\eta} \right) + \\ & \left. \left( \frac{n_{\mathbf{k}\nu} - n_{\mathbf{k}\nu'}}{\omega_{\mathbf{k}\nu'} - \omega_{\mathbf{k}\nu} - \omega - i\eta} \right) \right], \quad (6.8) \end{aligned}$$

which is the frequency- and temperature- dependent generalization of the zero-temperature lifetime result already described. It is derived in detail in Refs. [6]. The summation includes mode frequencies,  $\omega_{\mathbf{k}\nu}$ , and Bose occupation factors,  $n_{\mathbf{k}\nu}$ .

The real and imaginary parts of the self-energy for GaAs at 300 K are plotted in Figures 6.5 and 6.6. The calculations represent evaluation of the real and imaginary parts of Eq.6.8, with the Dirac delta function simulated with a Lorentzian, as discussed in Chapter 5. The real and imaginary parts show characteristics expected of two functions related to one

another by a Kramers-Kronig transformation.

## 6.4 Discussion

In Figure 6.1, along with the theoretical and experimental values for the absorption coefficient, the density of zero-momentum two-phonon states are also plotted for comparison with the absorption features. In Figure 6.7, the calculated phonon dispersion for each material is plotted.

The dispersion-oscillator-two-phonon quasiparticle model adopted is shown to agree remarkably well with the experimental absorption near the reststrahl and qualitatively away from it. The arrows in Figure 6.1 represent a few sum-process critical points as identified in the caption. The wave vectors are indicated with the standard notation for the high-symmetry points of a face-centered cubic reciprocal lattice, and the branches are labeled L(T)A(O) for longitudinal (transverse) and acoustic (optical). The three most energetic modes are denoted optical, the doubly degenerate modes are denoted transverse, and the singlets are denoted longitudinal. The identified two-phonon overtones are identical for each material, with the exception of the optical overtone at  $L$ , where the singlet is more energetic in GaP, and the reverse is true for GaAs, as can be seen in Figure 6.7. The doublet overtone is indicated for GaAs, and the singlet for GaP. The longitudinal-transverse band crossing in GaAs is a result of its similar ionic masses, as discussed below. The slight overbending, presumably, is an artifact of the calculation.

Above the reststrahlen, the theory reproduces spectral structure better than it does overall amplitude in the absorption. In the measurements, the relative absorption is more reliable than its absolute value [35]. It may be that the two-phonon features are not completely described through the infrared-active phonon self energy, and that direct multiphonon transitions should be considered. As can be seen from Eq. 6.8, our model cannot give absorption above  $2\omega_{TO}$ , where three-phonon and higher-order processes must be considered [36].

The temperature dependence of the absorption below  $100\text{ cm}^{-1}$  is ascribable to difference processes, where a phonon is absorbed and one of the same momentum but differing branch is emitted. Such processes are expressed in the third and fourth terms on the right side of Eq. 6.8, and are only possible at temperatures corresponding to finite phonon occupation numbers. The absorption grows as the material heats and the occupation numbers increase, and this behavior has been measured in GaAs for three far-infrared frequencies [37].

The GaP spectrum possesses a richer two-phonon structure than that of GaAs, including narrow bands of weak absorption, a consequence of its larger ionic mass mismatch, which widens the energy difference between various phonon branches. In the case of similar masses, such as those in GaAs, the optical and acoustic branches approach near degeneracy at high-symmetry wave vectors, thus narrowing the gap between the bands associated with the branches. The same is true for the transverse and longitudinal optical branches, which, in the case of GaAs, show greater dispersion and again nearly degenerate behavior at high-symmetry points. These effects can be seen through comparison of phonon densities of states of Figure 6.1 and in the dispersions of Figure 6.7, as well as through comparison of the absorption. The primary transparency band calculated for GaP, just below  $700\text{ cm}^{-1}$ , is observed. Although this trough in the absorption appears weak next to the sharp infrared-active phonon feature, it constitutes a local variation in the absorption by two orders of magnitude. For both materials, spectral structure is also evident in the temperature-dependent far-infrared absorption below the reststrahlen, where critical points can be seen in the theoretical plots.

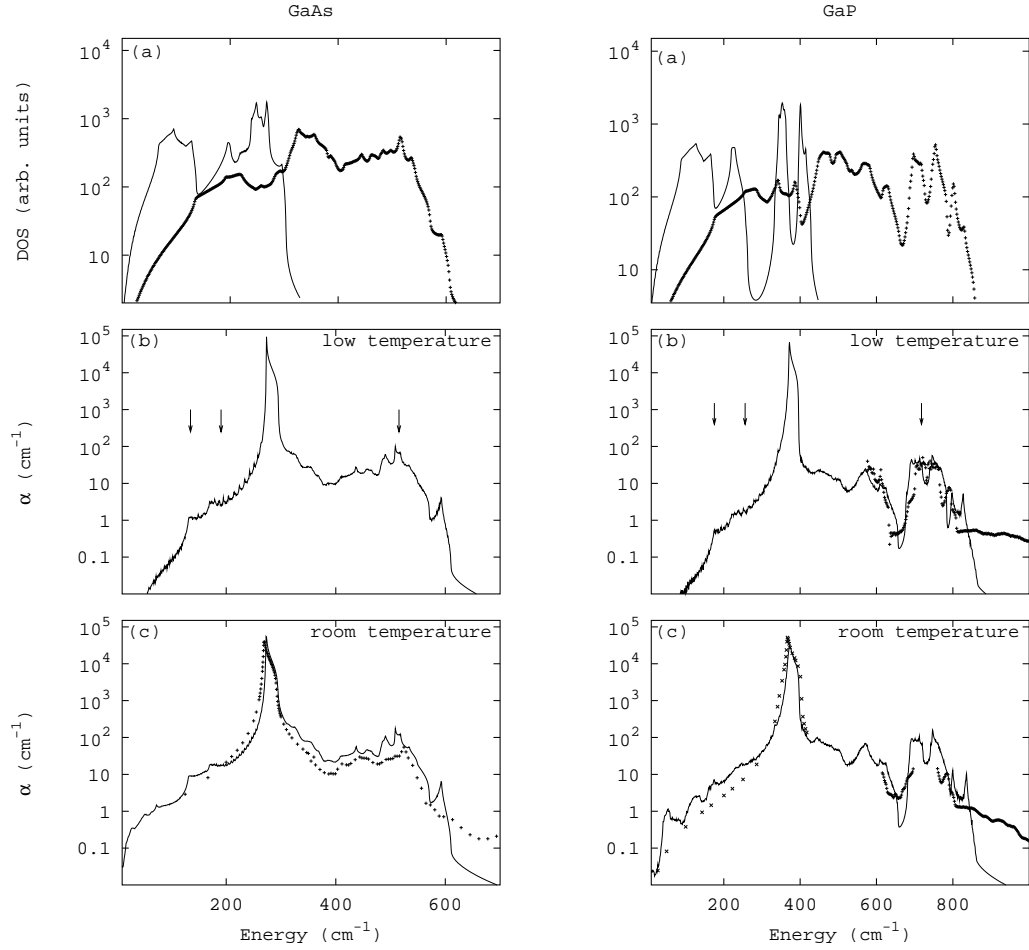


Figure 6.1: The one-phonon (line) and zero-momentum two-phonon (+) densities of states are plotted in (a) for GaAs to the left, and GaP to the right. In (b) and (c) the calculated absorption coefficient is plotted at  $< 10$  K and 300 K, respectively. Plotted theoretical spectral features have been moved to 0.97 of their calculated position, in  $\text{cm}^{-1}$ , to facilitate comparison with the experimental 300 K spectra, which are plotted in (c) (+). The arrows index, from left to right, the two-phonon critical points:  $TA(L) + TA(L)$ ,  $TA(X) + TA(X)$ , and  $TO(L) + TO(L)$ , with the exception of the overtone at  $L$ , as noted in the text. The data are from Refs. [33, 34, 35], as discussed in the text.

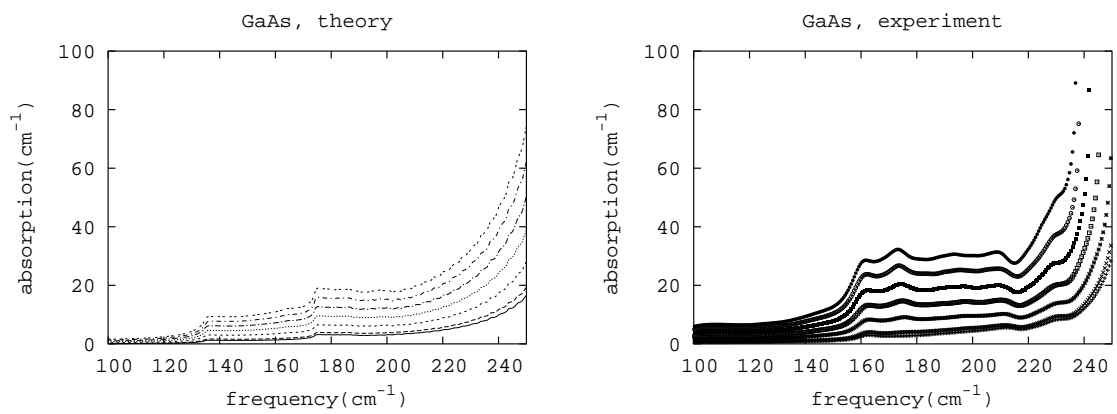


Figure 6.2: The experimental and calculated temperature dependence of far-infrared response in GaAs. The spectra are shown for the crystal at 10 K, 50 K, 100 K, 150 K, 200 K, 250 K, and 300 K. The absorption increases monotonically with temperature. The data were taken by Simon Kaplan at the National Institute of Standards and Technology.



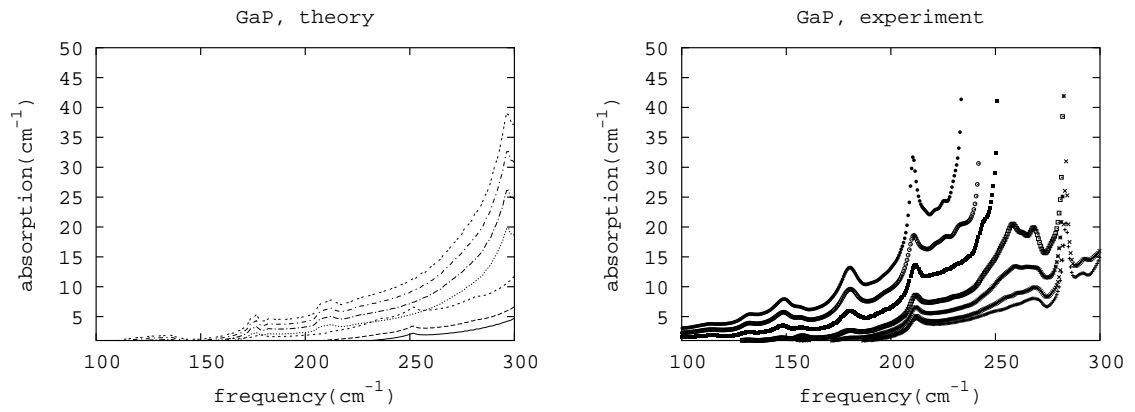


Figure 6.3: The experimental and theoretical temperature dependence of far-infrared response in GaP. The spectra are shown for the crystal at 10 K, 50 K, 100 K, 150 K, 200 K, 250 K, and 300 K. The absorption increases monotonically with temperature. The data were taken by Simon Kaplan at the National Institute of Standards and Technology.

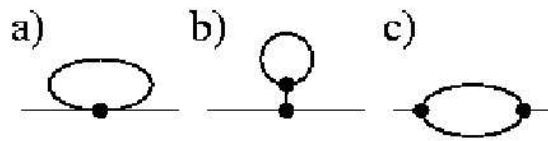


Figure 6.4: The vertex of diagram (a) represents a four-phonon interaction and is related to energy shifts associated with quartic terms in lattice strain. Diagram (b) expresses shifts associated with thermal expansion. Only diagram (c) contributes frequency dependence to the self-energy.

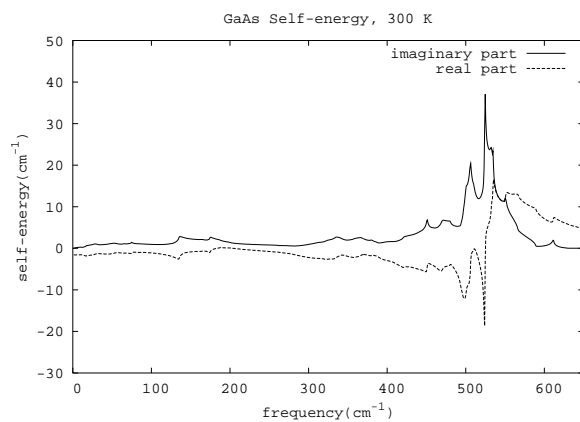


Figure 6.5: The calculated real and imaginary parts of the IR-active-phonon self-energy for GaAs at 300 K.

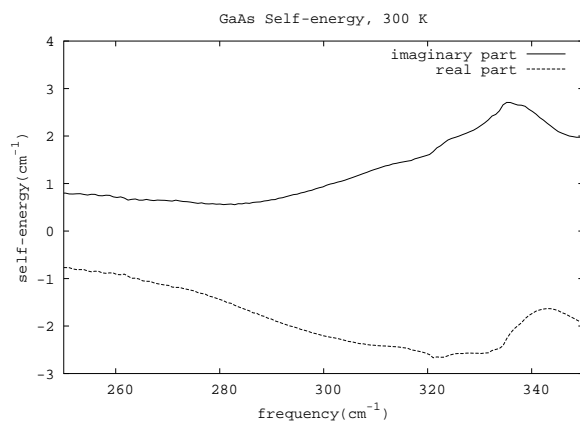


Figure 6.6: The calculated real and imaginary parts of the IR-active-phonon self-energy for GaAs at 300 K near the reststrahl.

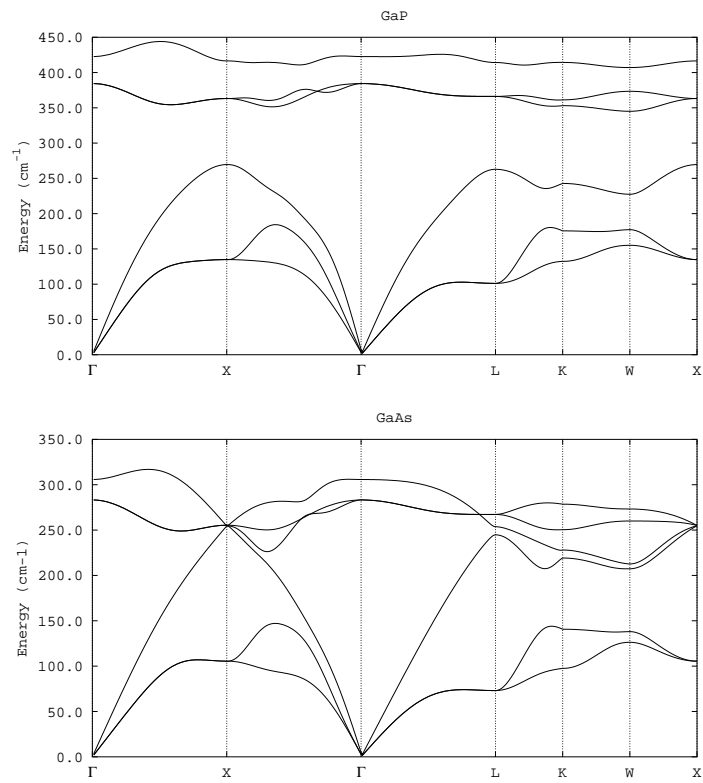


Figure 6.7: Phonon dispersion for GaAs and GaP.

## Chapter 7

# Ionic Displacement Correlations from the Zero-point Motion of Pressurized Solid Argon

## 7.1 The Correlation Function

Equal-time, ion-ion correlation functions have been of theoretical interest since the early days of theoretical lattice dynamics [51, 52]. The autocorrelations appear in the Debye-Waller factor and crystal melting criteria [53, 54], and the two-site correlations are related to a variety of measurable effects. They have been shown to imprint “extra spots” on the diffuse, elastic x-ray scattering background arising from thermal fluctuations [55, 56], and more recently, experiments concerning their relevance to extended x-ray absorption fine structure [57] and electronic motion [58] have been performed. Bond-charge models have been used to calculate a few of the correlations in covalent semiconductors [59].

Perhaps of particular theoretical interest, the correlation functions are relevant to lattice dynamics beyond the harmonic approximation. A body of theoretical work over the last five years marks a breakthrough in the first-principles considerations of anharmonic effects [8, 38, 41, 60], and the correlation functions can be applied to the calculation of related matrix elements. As an illustration of this, a term in the potential energy which is cubic in ionic displacements hybridizes the crystal’s ground state with a state in which a mode is occupied by a single phonon. The corresponding matrix element can be expressed as a phased sum of fourth-order correlations multiplied by appropriate anharmonic potential coefficients. These fourth-order correlations can be contracted into products of pairwise correlations over the ground state, which are evaluated here. In a related connection between anharmonic perturbation theory and the correlation functions, van Hove posited the ratio

of the autocorrelation length to ion separation as the expansion parameter with which to rank the multiphonon processes [49].

Commonly, the zero-point ionic motion's greatest experimental significance is in the study of the lightest elements, and would not be prominent in a system such as argon. However, at zero temperature, non-zero values of the correlation functions can generally be attributed solely to the quantum-mechanical zero-point motion of the ground state.

Ground-state correlations in solid argon are calculated here, for arbitrary lattice-site separation, using 1) current first-principles methods, and 2) analytic expressions from long-known approximations to the phonon spectrum [52]. Argon is a convenient choice for the calculation of these correlations. It is an insulating crystal with a single atom in the unit cell, and so complications associated with optical phonons and a Fermi surface need not be addressed. A comparison of results obtained via the two approaches is interesting as a mutual check on the modern technique, where the results are highly numeric in nature, and the more traditional analytic methods, which are computationally transparent but rely on more approximate assumptions.

## 7.2 Pressurized Solid Argon

Advanced spectroscopic techniques probing materials at high pressure have recently allowed detailed experimental investigation of structural properties of solid argon [61, 62, 63, 64], which is of interest as a fundamental solid. The equation of state and the pressure dependence of elastic constants and phonon dispersion have been reported. These investigations and accompanying pair-potential calculations have been complemented by first-principles studies which rely on local and semi-local approximations to density-functional theory [65, 66, 67, 68, 69]. There is general agreement between the theoretical and experimental results, and the degree of correspondence increases at higher pressures. This may be expected, since local and semi-local functionals account for electronic correlations only when

there is charge-density overlap, and hence cannot model strict van der Waals effects [65], and at lower densities, or lower pressures, the relative importance of the van der Waals forces obviously grows. Recently, functionals capable of treating van der Waals interactions have been developed [70].

Nevertheless, the theoretically obtained properties are reasonable even to nearly ambient pressure when the generalized-gradient functional is employed. The local-density approximation [10], with which the present results are calculated, has been shown to give an equation of state of poorer agreement with measurement than the generalized-gradient approximation [66]. Indeed, at lower pressures, the associated densities reported here are 10 % to 15 % higher than those obtained from experiment. In addition to the local-density approximation, these calculations are performed with pseudopotentials and a plane-wave basis [13, 14, 15]. All values reported were checked for convergence with respect to Brillouin-zone sampling and plane-wave cutoff.

The pressures are evaluated by first calculating points along a total-energy-vs-volume curve, and then obtaining a best fit to the Murnaghan equation of state. At 3.1 GPa and 6.7 GPa, the values are checked by introducing an internal strain. When the solid is pressurized, the energy density,  $E$ , is modified from its equilibrium value,  $E_0$ , by a linear as well as quadratic term with the uniaxial strain parameter  $e_{11}$ ,  $E = E_0 - Pe_{11} + \frac{1}{2}c_{11}e_{11}^2$ . The coefficient  $c_{11}$  in the quadratic term is the standardly defined elastic constant. The linear term represents work done as the volume varies with the strain, and the coefficient,  $P$ , represents the pressure. The pressures obtained from the strain calculation and from the equation of state agree to within 10 %.

### 7.3 Phonon Dispersion and Elastic Constants

The phonon dispersion is calculated through a diagonalization of the dynamical matrix, which is calculated with Hellmann-Feynman forces [18] and density-functional theory. Su-

percells with wave-commensurate geometries are utilized. Figure 7.1 displays theoretical phonon dispersion along a few high-symmetry lines for a crystal at 3.1 GPa, and how it compares to experimental dispersion along the (100) direction at the same pressure. The uncertainty in the experimental data points is less than  $\pm 1$  meV. The present result and the discrepancy from experiment is quite similar to that of other recently-reported work within the local-density approximation [66]. The theoretical density reported here is  $2.7 \text{ g/cm}^3$ . At 6.7 GPa, or a density of  $3.0 \text{ g/cm}^3$ , the frequency of the longitudinal mode at the Brillouin zone boundary along (100) increases to 26 meV from the value 21 meV at 3.1 GPa. At 10 GPa and 70 GPa, the value is respectively 29 meV and 53 meV, and the corresponding densities are  $3.2 \text{ g/cm}^3$  and  $4.6 \text{ g/cm}^3$ .

The elastic constants are reported through evaluation of the low-momentum speeds of sound from the calculated dispersion relations. At 6.7 GPa, the constants are computed twice. The second method entails monitoring of the total energy over a range of internal strains. The two values are identical to the numerical accuracy reported for  $c_{11}$ , and differ by about 20 % for  $c_{12}$  and  $c_{44}$  (for  $c_{12}$  the strain-derived value is lower, and for  $c_{44}$  the strain-derived value is higher). The calculated elastic constants for various crystal pressures are  $c_{11} = 36 \text{ GPa}$ ,  $c_{12} = 24 \text{ GPa}$ , and  $c_{44} = 16 \text{ GPa}$  at 3.1 GPa;  $c_{11} = 54 \text{ GPa}$ ,  $c_{12} = 38 \text{ GPa}$ , and  $c_{44} = 23 \text{ GPa}$  at 6.7 GPa;  $c_{11} = 72 \text{ GPa}$ ,  $c_{12} = 50 \text{ GPa}$ , and  $c_{44} = 33 \text{ GPa}$  at 10 GPa; and  $c_{11} = 270 \text{ GPa}$ ,  $c_{12} = 200 \text{ GPa}$ , and  $c_{44} = 130 \text{ GPa}$  at 70 GPa. These values for the elastic constants differ from those of some earlier studies by more than 50 % at 3.1 GPa. The agreement improves at higher pressures to about 10 % at 70 GPa.

## 7.4 Exact Formulas for the Correlation Function

The displacement of an ion at lattice site  $\mathbf{R}$  along Cartesian direction  $i$  is written as the sum over phonon creation and annihilation operators, indexed by wave vector and branch:

$$x_{i\mathbf{R}} = \frac{1}{\sqrt{N}} \sum_{\mathbf{k}\nu} e^{i\mathbf{k}\cdot\mathbf{R}} \sqrt{\frac{\hbar}{2m\omega_{\mathbf{k}\nu}}} (a_{\mathbf{k}\nu} + a_{-\mathbf{k}\nu}^\dagger) u_{\mathbf{k}\nu i}, \quad (7.1)$$

where the right-hand side makes reference to phonon polarization, and to square roots of the ionic mass, phonon frequency, and number of lattice sites (or independent wave vectors) in the denominators.

The ground-state expectation value of the product of two such operators, defined to be the ground-state ion-ion correlation, is:

$$\langle x_{i\mathbf{R}+\mathbf{S}} x_{j\mathbf{R}} \rangle = \frac{1}{N} \sum_{\mathbf{k}\nu} e^{i\mathbf{k}\cdot\mathbf{S}} \frac{\hbar}{2m\omega_{\mathbf{k}\nu}} u_{\mathbf{k}\nu i} u_{\mathbf{k}\nu j}^*, \quad (7.2)$$

because only terms first creating and then annihilating the same phonon are nonzero, and because of the relation,  $u_{-\mathbf{k}\nu} = u_{\mathbf{k}\nu}^*$ . The vectors  $\{\mathbf{u}_{\mathbf{k}\nu}\}$  form an orthonormal, diagonal basis for the dynamical matrix  $\mathbf{D}(\mathbf{k})$ , and its eigenvalues are the squares of the phonon frequencies, implying the relations

$$\sum_{\nu} \frac{u_{\mathbf{k}\nu i} u_{\mathbf{k}\nu j}^*}{\omega_{\mathbf{k}\nu}} = \left( D^{-\frac{1}{2}}(\mathbf{k}) \right)_{ij},$$

and

$$\langle x_{i\mathbf{R}+\mathbf{S}} x_{j\mathbf{R}} \rangle = \frac{\hbar}{2mN} \sum_{\mathbf{k}} e^{i\mathbf{k}\cdot\mathbf{S}} \left( D^{-\frac{1}{2}}(\mathbf{k}) \right)_{ij}. \quad (7.3)$$

The result is that the dynamical matrix contains all the information necessary to calculate the ion-ion correlation functions.

## 7.5 Approximate Formulas

A cautious analysis of the correlations benefits from an analytic check on the numeric results derived from the above expressions. The primary concern with the numerical results is the



singularity which occurs in Eq. 7.3 as  $\mathbf{k}$  tends to zero. Further, the coherent nature of the contributions to the correlations from small-momentum wave vectors may indicate sensitivity to the sampling about the  $\Gamma$  point. For these reasons, as well as for the sake of comparing exact and heavily computational results with common approximations in handling the phonon spectrum, such as the Debye model, systematic analysis of the correspondence between the two is performed. The comparison also provides a measure of anisotropy's effect on the correlations.

Three approximations bridge the transition from the expression in Eq. 7.3 to an analytically treatable case. Two of the approximations are well known from the Debye model: taking the acoustic, small-momentum linear dispersion as valid throughout the whole Brillouin zone; and approximating the Brillouin zone itself as a sphere of the same volume. The third approximation forces an isotropic condition on the elastic constants.

The linear-dispersion approximation can be expressed through examination of the small-momentum expansion of the dynamical matrix. Considering the Cartesian components of a deformation field  $u_i(\mathbf{R})$  within the crystal, and the deformations vary slowly, the local energy density of a cubic system can be written [71]:

$$U = \frac{1}{2}c_{11} \sum_i \left( \frac{\partial u_i}{\partial R_i} \right)^2 + \frac{1}{2}c_{44} \sum_i \sum_{j < i} \left( \frac{\partial u_i}{\partial R_j} + \frac{\partial u_j}{\partial R_i} \right)^2 + c_{12} \sum_i \sum_{j < i} \frac{\partial u_i}{\partial R_i} \frac{\partial u_j}{\partial R_j}. \quad (7.4)$$

Slowly varying deformations can be treated with a continuum model, where the Fourier transform of the strain field is defined,

$$u_i(\mathbf{k}) = \frac{1}{\Omega_0} \int d^3\mathbf{r} u_i(\mathbf{r}) e^{-i\mathbf{k}\cdot\mathbf{r}}, \quad (7.5)$$

and  $\Omega_0$  is the crystal volume. The dynamical matrix is,

$$D_{ij}(\mathbf{k}) = \frac{1}{\rho} \frac{\partial^2 U}{\partial u_i(-\mathbf{k}) \partial u_j(\mathbf{k})}, \quad (7.6)$$

where  $\rho$  is the mass density, and the eigenvalues of the dynamical matrix are the squares of the phonon frequencies. Working out the equations of motion from Eq. 7.4, the small-

momentum dynamical matrix for acoustic phonons is:

$$\mathbf{D}(\mathbf{k}) = \frac{1}{\rho} \begin{pmatrix} c_{11}k_x^2 + c_{44}(k_y^2 + k_z^2) & (c_{12} + c_{44})k_x k_y & (c_{12} + c_{44})k_x k_z \\ (c_{12} + c_{44})k_x k_y & c_{11}k_y^2 + c_{44}(k_x^2 + k_z^2) & (c_{12} + c_{44})k_y k_z \\ (c_{12} + c_{44})k_x k_z & (c_{12} + c_{44})k_y k_z & c_{11}k_z^2 + c_{44}(k_x^2 + k_y^2) \end{pmatrix}. \quad (7.7)$$

The second approximation is that of an isotropic crystal:

$$c_{11} = c_{12} + 2c_{44}. \quad (7.8)$$

This condition reduces Eq. 7.7 to projections onto longitudinal and transverse modes:

$$\mathbf{D}(\mathbf{k}) = \frac{c_{11}k^2}{\rho} |\hat{\mathbf{k}}\rangle\langle\hat{\mathbf{k}}| + \frac{c_{44}k^2}{\rho} (1 - |\hat{\mathbf{k}}\rangle\langle\hat{\mathbf{k}}|), \quad (7.9)$$

and makes the speeds of sound independent of wave vector.

The third, Debye-like approximation defines a sphere of radius  $k_{DB}$  and replaces the Brillouin zone integration with integration over the sphere volume, implying

$$\frac{4\pi}{3}k_{DB}^3 = \Omega_{BZ}. \quad (7.10)$$

## 7.6 Analytical and Numerical Results at 6.7 GPa

Via the three approximations above, a stepwise transition is made from realistic argon to a model system with analytical expression of the correlation function. As each successive approximation is made, its effect on the correlation function is monitored by making a numerical calculation, and then performing the algebraic computation for the analytically treatable approximations. Numerical calculations are done for the following cases: 1) exact realistic calculation, 2) application of the small-momentum phonon spectrum, Eq. 7.7, and 3) and application of Eq. 7.7 and the isotropic crystal approximation, Eq. 7.8. The isotropic elastic constants are selected to meet Eq. 7.8, and to not affect their average value or that of the bulk modulus, giving  $c_{11} = 69$  GPa,  $c_{12} = 33$  GPa, and  $c_{44} = 18$  GPa.

When the substitution of a sphere for the actual Brillouin zone is joined with the conditions Eqs. 7.7 and 7.8, Eq. 7.3 becomes:

$$\langle x_{i\mathbf{R}+\mathbf{S}}x_{j\mathbf{R}} \rangle = \frac{\hbar}{2m\Omega_{BZ}} \int d^3\mathbf{k} e^{i\mathbf{k}\cdot\mathbf{S}} \frac{\sqrt{\rho}}{k^3} \left( \frac{k_i k_j}{\sqrt{c_{11}}} + \frac{k^2 \delta_{ij} - k_i k_j}{\sqrt{c_{44}}} \right). \quad (7.11)$$

The integration is performed over the sphere of Eq. 7.10. Making the following definitions

$$\begin{aligned} \phi &= k_{DB}S, \\ \alpha_i &= 1 - \left( \frac{S_i}{S} \right)^2, \\ \gamma_{ij} &= \frac{S_i S_j}{S^2}, \\ \frac{1}{c} &= \sqrt{\rho} \left( \frac{1}{\sqrt{c_{11}}} - \frac{1}{\sqrt{c_{44}}} \right), \end{aligned}$$

and performing the integration, the result for  $i = j$  is,

$$\begin{aligned} \langle x_{i\mathbf{R}+\mathbf{S}}x_{i\mathbf{R}} \rangle &= \\ \frac{\hbar}{2m\Omega_{BZ}} \frac{4\pi}{S^2} &\left( \sqrt{\frac{\rho}{c_{44}}} (1 - \cos \phi) + \frac{1}{c} \left( 2\alpha_i - 1 + (\alpha_i - 1) \cos \phi + (2 - 3\alpha_i) \frac{\sin \phi}{\phi} \right) \right), \end{aligned} \quad (7.12)$$

and for  $i \neq j$  the result is,

$$\langle x_{i\mathbf{R}+\mathbf{S}}x_{j\mathbf{R}} \rangle = \frac{\hbar}{2m\Omega_{BZ}c} \frac{4\pi}{S^2} \gamma_{ij} \left( \frac{3\sin \phi}{\phi} - \cos \phi - 2 \right). \quad (7.13)$$

Figures 7.2 and 7.3 represent the non-zero correlations between ions with separations that lie in the indicated directions for a crystal held at a pressure of 6.7 GPa. (The correlation is zero whenever  $\hat{\mathbf{x}}_j$  has no projection in the  $\hat{\mathbf{x}}_i$ - $\mathbf{S}$  plane.) Four results are plotted representing the sequential approximation from the real crystal to the analytically amenable idealization. The first three plotted results are numerically calculated, and the final result is analytical. The plots are for the actual crystal at 6.7 GPa, and the three successively imposed conditions: use of the small-momentum rather than the full form of the dynamical matrix, use of an isotropic set rather than the real set of elastic constants, and use of a sphere rather than the actual Brillouin zone. In imposing the last condition, the transition to the idealization is complete.

For demonstration of the extent of agreement between the four cases, separation distance between ions is treated as a continuous quantity. The first few actual site-separation distances are indicated with arrows.

## 7.7 Pressure Dependence of the Correlation Function

The correlations are immediately associated with a length by taking their square root. In Figure 7.4 the dimensionless ratio of the correlation length to the nearest-neighbor distance is plotted with the dimensionless, normalized ion-ion separation along the (110) direction. The figure corresponds to the exact calculation, Eq. 7.3. Actual lattice sites are represented by the ticks in the figure. The delocalization length associated with the autocorrelation decreases from from 2 % to 1.5 % of the nearest-neighbor distance as the pressure is increased from 3.1 GPa to 70 GPa. This result, together with van Hove's ansatz, suggests that ground-state anharmonic effects are less important at higher pressure. This conjecture is motivated by recognizing that the higher-order correlations—which are proportional to products of lower-order correlations—must diminish more quickly than the pair correlations. Therefore, as the pair correlations decrease, the ions are less and less subject to the anharmonic forces associated with displacements appearing in the higher-order correlations. This is a familiar many-body result, where perturbations rise less rapidly than confinement energy as the density is increased.

## 7.8 Conclusions

This study of the pressure dependence of the lattice dynamics and elastic properties of solid argon confirms earlier findings that the local-density approximation is problematic at low pressures, and improves at high pressures. Structural calculations are extended to the ion correlation function. The analytical and exact results correspond as well as

may be expected, and straightforward numerical approaches appear sufficient in spite of concerns about sensitivity to sampling near the  $\Gamma$  point. The impact of the small-momentum approximation is the largest among the three, and tends to suppress the autocorrelation function by approximately 20 %. At the same lattice vector, the correlations for varying displacement orientations are of the same order (where not zero by symmetry). While there is an order of magnitude decrease from the autocorrelation to that of the nearest neighbors, the dimensionless parameter associated with the correlation decays more slowly, from 2 % for the on-site correlation to just under 1 % for nearest ions at 6.7 GPa. Roughly similar behavior with increasing lattice vector is demonstrated at other pressures. The dimensionless correlation parameter associated with the autocorrelation is about 2 % at 6.7 GPa, and falls to about 1.5 % at 70 GPa. This suggests that the anharmonic nature of the crystal's ground state is suppressed at higher pressures.

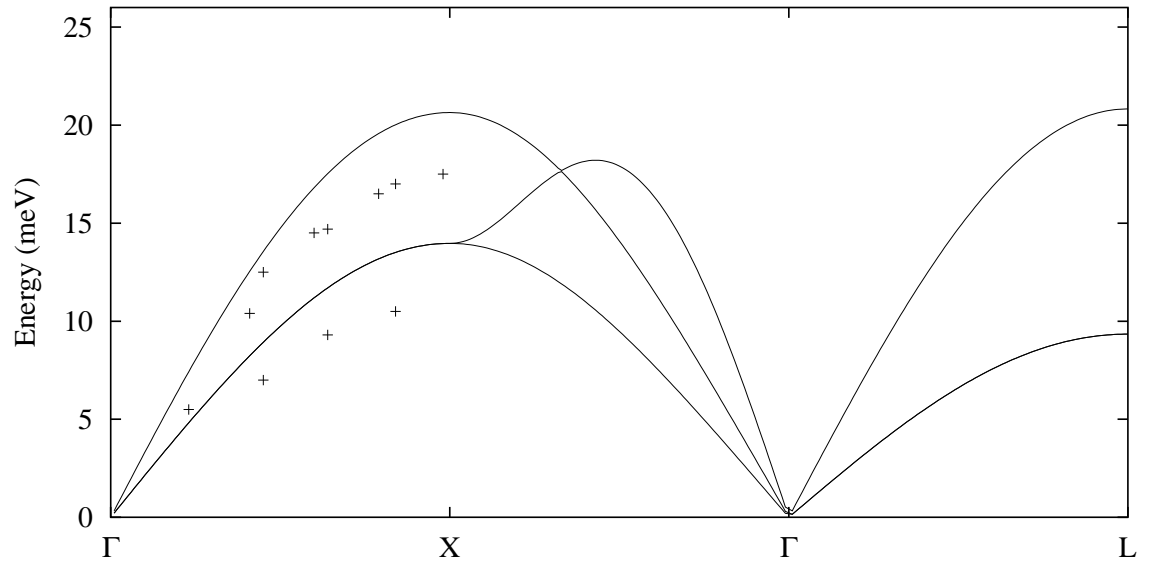


Figure 7.1: Dispersion along a few high-symmetry lines (lines), and experimental data from Ref [61] (points).

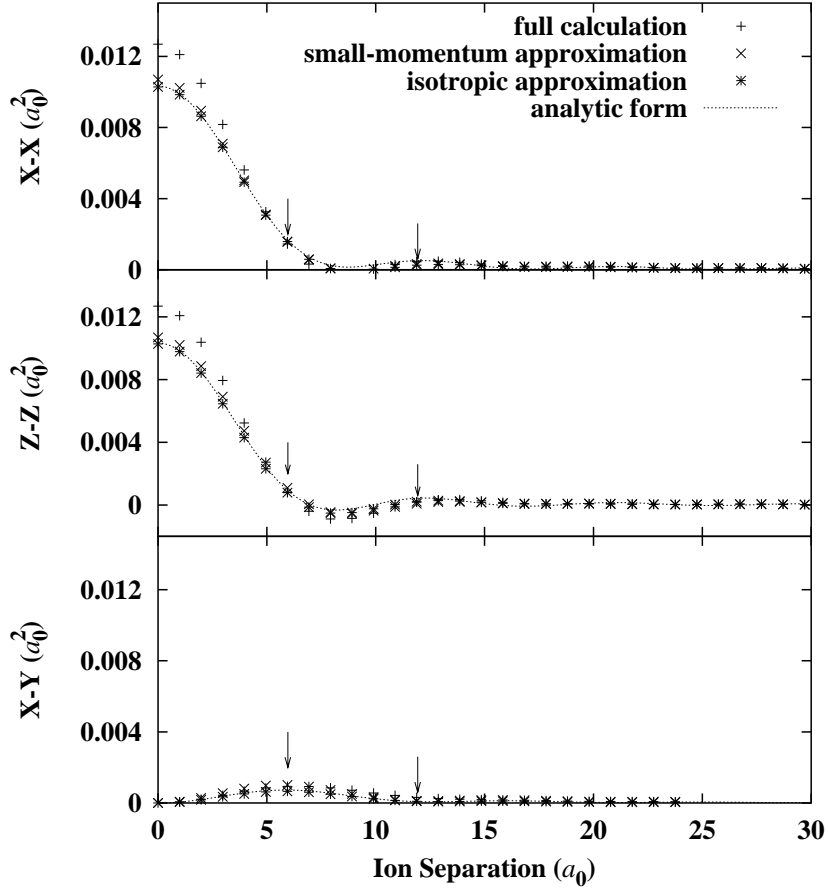


Figure 7.2: Plots are for correlations, with ion separation along (110), in which both ions are displaced along the x direction (top), for both ions displaced along the z direction (middle), and for one ion displaced along the x direction and the other along the y direction (bottom). Correlations for orientations not shown are zero by symmetry or symmetry-equivalent to those shown. The nearest sites are represented by arrows. The crosses represent the full calculation and the dashed line represents the analytical result. The intermediate approximations are represented by the stars (small-momentum approximation), and by the diagonal crosses (small-momentum approximation and isotropic approximation).

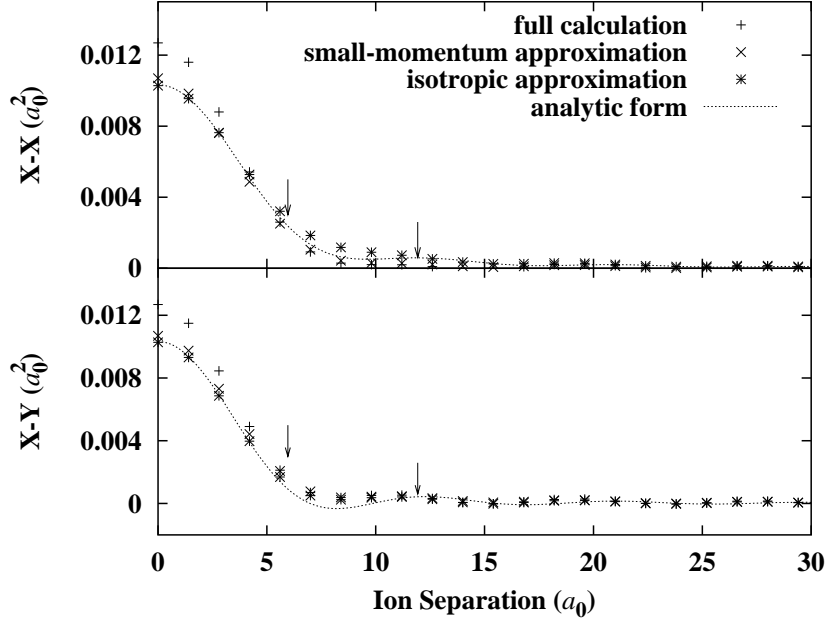


Figure 7.3: Plots are for correlations, with ion separation along (200), in which both ions are displaced along the x direction (top), and for one ion displaced along the x direction and the other along the y direction (bottom). Correlations for orientations not shown are zero by symmetry or symmetry-equivalent to those shown. The nearest sites are represented by arrows. The crosses represent the full calculation and the dashed line represents the analytical result. The intermediate approximations are represented by the stars (small-momentum approximation), and by the diagonal crosses (small-momentum approximation and isotropic approximation).



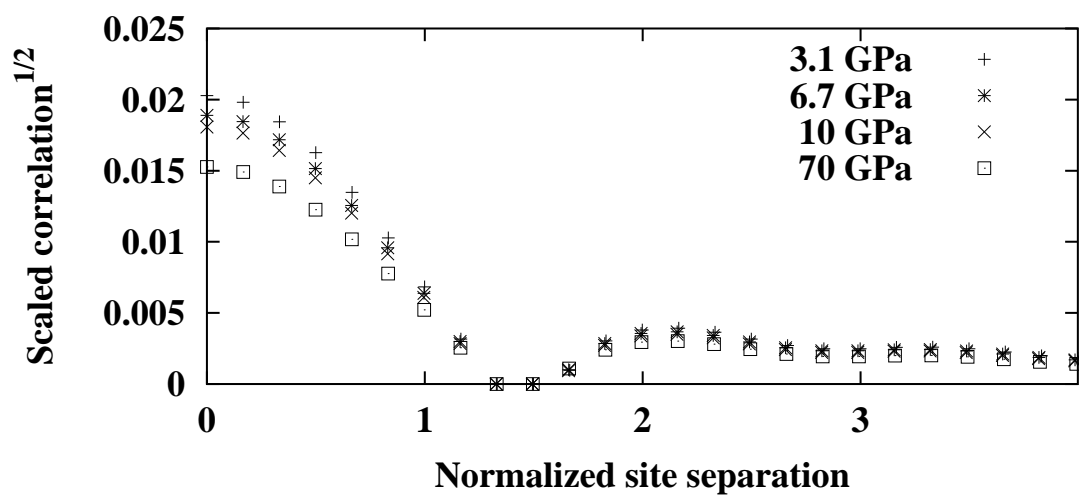


Figure 7.4: The square root of the x-x correlation function plotted with ion separation along the (110) direction, both normalized to nearest neighbor distance, for various pressures. The ticks represent actual lattice sites.

## Chapter 8

### Conclusions

The scheme of the *ab initio* calculations reported in this thesis can be summarized with the following: 1) pseudopotentials are calculated in the limit of isolated atoms; 2) the pseudopotentials are employed in solid-state calculations, which give Born-von Karman force constants and anharmonic terms; 3) the force constants are interpolated over the Brillouin zone for the evaluation of phonon spectra and self-energies.

Innovations in phonon spectra and anharmonic matrix elements calculations are reported, and the results are similar to other first-principles methods in their agreement with experimental phonon frequencies and lifetimes. The phonon self-energy and Born-effective charges are applied to an *ab initio* calculation of the frequency and temperature dependence of the infrared dielectric response of bulk GaAs and GaP, and the agreement with agreement suggests microscopic validity of the model. The gain in insight and computational power may prove useful in the infrared characterization of defects in materials, the study of semiconductor heating, the engineering of infrared sensors, and the design of infrared components.

There are several directions for theoretical advancement of the results. One is the incorporation of direct two-phonon interactions with light, or higher-order charges, in the calculation. These charges co-exist with the anharmonic two-phonon oscillator strength, calculated through the admixture with the optical phonon, as discussed in Chapter 6. One approach to the calculation of the two-phonon charges is frozen-two-phonon calculations combined with the modern theory of polarization.

Calculating the anharmonic interactions of three-phonon states with the optical phonon may also improve the theory. These processes contribute a signature temperature

dependence of the absorption, and allow for the calculation of the absorption above twice the optical-phonon frequency. Two essential pieces to this accomplishment are the identification and derivation of appropriate three-phonon Green's functions, and the calculation of three-phonon-optical-phonon interaction vertices. A possible strategy for calculating the vertices may start with supercells which are simultaneously wave-commensurate with two wave vectors. Geometrically, such a supercell must also be wave-commensurate with a third wave vector,  $\mathbf{k}_3$ , satisfying  $\mathbf{k}_3 = \mathbf{k}_2 - \mathbf{k}_1$ . Thus, such a supercell would be amenable to frozen-three-phonon calculations. The quartic terms relevant to the three-phonon-optical-phonon vertices can be evaluated through the change in three-phonon potential energy terms with respect to sublattice displacement. Another possible tactic for calculating the three-phonon vertices is the combination of frozen-phonon calculations and density-functional perturbation theory.

A further application of the present methods may be the calculation of the polarization—as well as frequency and temperature—dependence of the infrared response in polar, non-cubic crystals, such as wurzite GaN or graphite. In such a crystal, several symmetry-independent IR-active phonons may coexist, each with their own Born-effective charges and self-energies. The response for various photon polarizations may then be calculated.

The calculations of ionic displacement correlations in Chapter 7 lead to the conjecture that anharmonic effects are less prominent at higher pressure. The anharmonic treatment of Chapter 5 is not a good test of this conjecture, because the tuning between the IR-active phonon energy and two-phonon features is also critical. A better theoretical test of the conjecture may be conducted, in a material like argon, through evaluation of the variation in Grüneisen parameters with pressure.

## Appendix A

### Fitting and Interpolation Algorithm

In Chapter 3, it was mentioned that the inter-atomic force constants, which allow interpolation from the dynamical matrix, are obtained with a least-squares fit, subject to symmetry constraints and the acoustic sum rule. Details of this procedure are provided here.

The Born-Oppenheimer energy surface of a lattice is given by  $V(\{\mathbf{x}_\tau(\mathbf{R})\})$ , where  $\mathbf{x}_\tau(\mathbf{R})$  denotes the displacement from equilibrium of the atom located at  $\mathbf{R} + \mathbf{s}_\tau$ , or at basis vector  $\mathbf{s}_\tau$  indexed by  $\tau$  in the cell specified by the lattice vector  $\mathbf{R}$ . The matrices,  $\{\mathbf{C}_{\tau\tau'}(\mathbf{R})\}$ , are the  $3 \times 3$  matrices denoting the IFCs. They satisfy

$$V(\{\mathbf{x}_\tau(\mathbf{R})\}) = V_0 + \frac{1}{2} \sum_{\mathbf{S}, \mathbf{R}, \tau, \tau'} \mathbf{x}_\tau^T(\mathbf{S}) \cdot \mathbf{C}_{\tau\tau'}(\mathbf{R}) \cdot \mathbf{x}_{\tau'}(\mathbf{S} + \mathbf{R}) + \dots$$

Because of crystal symmetry, there are simple symmetry relationships between interatomic-force constants. Let  $\mathbf{U}_n$  be a symmetry operator of the crystal group (i.e., a  $3 \times 3$  proper or improper rotation matrix) indexed by  $n$ , which satisfies,

$$\mathbf{U}_n \mathbf{s}_\tau = \mathbf{s}_\sigma + \mathbf{g}_n + \mathbf{R}(\mathbf{U}_n, \mathbf{s}_\tau) \quad (\text{A.1})$$

$$\mathbf{U}_n \mathbf{s}_{\tau'} = \mathbf{s}_{\sigma'} + \mathbf{g}_n + \mathbf{R}(\mathbf{U}_n, \mathbf{s}_{\tau'}). \quad (\text{A.2})$$

$$\mathbf{R}' = \mathbf{U}_n \mathbf{R} + \mathbf{R}(\mathbf{U}_n, \mathbf{s}_{\tau'}) - \mathbf{R}(\mathbf{U}_n, \mathbf{s}_\tau), \quad (\text{A.3})$$

where  $\mathbf{g}_n$  is the glide associated with  $\mathbf{U}_n$ ,  $\mathbf{s}_\tau$  is the atomic position of the  $\tau^{\text{th}}$  atom relative to a Bravais lattice site and,  $\mathbf{R}(\mathbf{U}_n, \mathbf{s}_\tau)$ ,  $\mathbf{R}'$ , and  $\mathbf{R}$  are lattice vectors. The basic symmetry transformation relating interatomic force constants is

$$(\mathbf{U}_n \mathbf{e}_a)^T \cdot \mathbf{C}_{\sigma\sigma'}(\mathbf{R}') \cdot (\mathbf{U}_n \mathbf{e}_b) = \mathbf{e}_a^T \cdot \mathbf{C}_{\tau\tau'}(\mathbf{R}) \cdot \mathbf{e}_b, \quad (\text{A.4})$$

where  $\mathbf{e}_a$  and  $\mathbf{e}_b$  are unit-vectors in Cartesian directions labeled by the indices  $a$  and  $b$ .

We may call the triplets  $(\mathbf{R}, \tau, \tau')$  and  $(\mathbf{R}', \sigma, \sigma')$  symmetry equivalent if they satisfy Eqs. A.1, A.2, and A.3, for some symmetry operation of the crystal group,  $\mathbf{U}_n$ . We may divide these triplets into triplet sets in which all of the members within the same set are symmetry equivalent. After we divide all the triplets into sets, we assign to each triplet an ordered pair,  $(j, i)$ , where  $j$  labels the set to which the triplet belongs, and  $i$  labels which member in the set the triplet corresponds to. There is then a one-to-one correspondence between the triplet  $(\mathbf{R}, \tau, \tau')$  and the ordered pair  $(j, i)$ .

We are interested in computing the general form of  $\mathbf{C}_{\tau\tau'}(\mathbf{R})$ , that is, finding a minimal set of  $3 \times 3$  basis matrices,  $\{\mathbf{F}_k, k = 1, \dots, M\}$ , in terms of which  $\mathbf{C}_{\tau\tau'}(\mathbf{R})$  can be generally expressed as a linear combination. That is, we have

$$\mathbf{C}_{\tau\tau'}(\mathbf{R}) = \sum_{k=1}^M a_k \mathbf{F}_k. \quad (\text{A.5})$$

To find  $\{\mathbf{F}_k, k = 1, \dots, M\}$ , we use the basic symmetry relation Eq. A.4, and other elementary properties of the matrix  $\mathbf{C}_{\tau\tau'}(\mathbf{R})$ , to form general constraints on  $\mathbf{C}_{\tau\tau'}(\mathbf{R})$ . We express these constraints as homogeneous linear equations that give us  $\{\mathbf{F}_k\}$ . Plainly we have

$$\frac{\partial^2 V}{\partial x_{\tau'b}(\mathbf{R}) \partial x_{\tau a}(\mathbf{0})} = \frac{\partial^2 V}{\partial x_{\tau a}(\mathbf{0}) \partial x_{\tau'b}(\mathbf{R})}, \quad (\text{A.6})$$

and

$$\frac{\partial^2 V}{\partial x_{\tau a}(\mathbf{S}) \partial x_{\tau'b}(\mathbf{R} + \mathbf{S})} = \frac{\partial^2 V}{\partial x_{\tau a}(\mathbf{0}) \partial x_{\tau'b}(\mathbf{R})}. \quad (\text{A.7})$$

Eq. A.6 is the equality of mixed partials, and Eq. A.7 results from the discrete translational symmetry of the crystal. Combining Eq. A.6 and Eq. A.7 and setting  $\mathbf{S} = -\mathbf{R}$ , we obtain

$$\frac{\partial^2 V}{\partial x_{\tau'b}(\mathbf{0}) \partial x_{\tau a}(-\mathbf{R})} = \frac{\partial^2 V}{\partial x_{\tau a}(\mathbf{0}) \partial x_{\tau'b}(\mathbf{R})}. \quad (\text{A.8})$$

Combining the definition in Eq. 3.1 and Eq. A.8, we have

$$\mathbf{C}_{\tau'\tau}^T(-\mathbf{R}) = \mathbf{C}_{\tau\tau'}(\mathbf{R}). \quad (\text{A.9})$$

From this it follows that  $\tilde{\mathbf{C}}_{\tau\tau'}(\mathbf{k})$  is a Hermitian matrix, if taken as a  $3N \times 3N$  matrix, where  $N$  is the number of atoms in the unit cell. Because Eq. A.9 is equivalent to the Hermiticity of the reciprocal-space IFC  $\tilde{\mathbf{C}}_{\tau\tau'}(\mathbf{k})$ , we will refer to Eq. A.9 as the ‘‘Hermiticity condition.’’

For a given triplet  $(\mathbf{R}, \tau, \tau')$ , we define the *little group* and *transpose set* ( $L_{\mathbf{R},\tau,\tau'}$  and  $T_{\mathbf{R},\tau,\tau'}$ ) as follows.  $L_{\mathbf{R},\tau,\tau'}$  is the subgroup of the crystal group that transforms the triplet  $(\mathbf{R}, \tau, \tau')$  into itself.  $T_{\mathbf{R},\tau,\tau'}$  is the subset of the crystal group that transforms the triplet  $(\mathbf{R}, \tau, \tau')$  to  $(-\mathbf{R}, \tau', \tau)$ .  $T_{\mathbf{R},\tau,\tau'}$  may or may not be a group. From Eq. A.4, we have

$$\mathbf{C}_{\tau'\tau}(-\mathbf{R}) = \mathbf{U}_n^T \mathbf{C}_{\tau\tau'}(\mathbf{R}) \mathbf{U}_n, \mathbf{U}_n \in T_{\mathbf{R},\tau,\tau'}. \quad (\text{A.10})$$

Combining Eq. A.10 with the Hermiticity condition (Eq. A.9), we have

$$\mathbf{C}_{\tau\tau'}^T(\mathbf{R}) = \mathbf{U}_n^T \mathbf{C}_{\tau\tau'}(\mathbf{R}) \mathbf{U}_n, \mathbf{U}_n \in T_{\mathbf{R},\tau,\tau'}. \quad (\text{A.11})$$

This constrains the transpose of the real-space IFCs. In particular, if one has cubic symmetry, it implies that the diagonal blocks of the dynamical matrix must be symmetric. Further constraints can be imposed by the little group:

$$\mathbf{C}_{\tau\tau'}(\mathbf{R}) = \mathbf{U}_n^T \mathbf{C}_{\tau\tau'}(\mathbf{R}) \mathbf{U}_n, \mathbf{U}_n \in L_{\mathbf{R},\tau,\tau'}. \quad (\text{A.12})$$

Eq. A.11 defines the *transpose-set constraints*, and Eq. A.12 defines the *little-group constraints*. The next step is to exploit the above constraints toward finding the basis matrices,  $\{\mathbf{F}_k\}$ . Later, further constraints are introduced to enforce the acoustic sum rule.

We may define another set of  $3 \times 3$  basic matrices,  $\{\mathbf{B}_i, i = 1, 2, \dots, 9\}$ , as,

$$\mathbf{B}_1 = \hat{\mathbf{x}}\hat{\mathbf{x}}, \mathbf{B}_2 = \hat{\mathbf{y}}\hat{\mathbf{y}}, \mathbf{B}_3 = \hat{\mathbf{z}}\hat{\mathbf{z}},$$

$$\mathbf{B}_4 = \hat{\mathbf{y}}\hat{\mathbf{z}}, \mathbf{B}_5 = \hat{\mathbf{x}}\hat{\mathbf{z}}, \mathbf{B}_6 = \hat{\mathbf{x}}\hat{\mathbf{y}},$$

$$\mathbf{B}_7 = \hat{\mathbf{z}}\hat{\mathbf{y}}, \mathbf{B}_8 = \hat{\mathbf{z}}\hat{\mathbf{x}}, \mathbf{B}_9 = \hat{\mathbf{y}}\hat{\mathbf{x}}.$$

Here we employ the dyadic notation whereby  $\hat{\mathbf{z}}\hat{\mathbf{y}}$  denotes a  $3 \times 3$  matrix with all zero entries except for a 1 in the 3rd row and 2nd column. We may define the scalar product of two  $3 \times 3$  matrices in terms of the basic matrices,

$$\langle \mathbf{B}_i, \mathbf{B}_j \rangle = \delta_{ij}. \quad (\text{A.13})$$

We define the entries of the  $9 \times 9$  matrices,  $\mathbf{S}$ , and  $\mathbf{M}(n)$ , by,

$$S_{ij} = \langle \mathbf{B}_i, \mathbf{B}_j^T \rangle \quad (\text{A.14})$$

and

$$M_{ij}(n) = \langle \mathbf{B}_i, \mathbf{U}_n^T \mathbf{B}_j \mathbf{U}_n \rangle. \quad (\text{A.15})$$

If we express  $\mathbf{C}_{\tau\tau'}(\mathbf{R})$  as a linear combination of the nine basic matrices, i.e., as

$$\mathbf{C}_{\tau\tau'}(\mathbf{R}) = \sum_{i=1}^9 \alpha_i \mathbf{B}_i, \quad (\text{A.16})$$

the little-group constraints (Eq. A.12) become

$$\sum_{j=1}^9 (M_{ij}(n) - \delta_{ij}) \alpha_j = 0, \mathbf{U}_n \in L_{\mathbf{R},\tau,\tau'}, \quad (\text{A.17})$$

and the transpose-set constraints (Eq. A.11),

$$\sum_{j=1}^9 (M_{ij}(n) - S_{ij}) \alpha_j = 0, \mathbf{U}_n \in T_{\mathbf{R},\tau,\tau'}. \quad (\text{A.18})$$

If there are  $N_L$  operations in the little group and  $N_T$  operations in the transpose set, there are a total of  $N' = 9(N_L + N_T)$  constraint equations, not all of which are independent. Let us define a set of  $N'$  9-component vectors,  $\{\beta^{(n)}, n = 1, \dots, N'\}$ , such that the system of equations,

$$\sum_{i=1}^9 \beta_i^{(n)} \alpha_i = 0, n = 1, \dots, N', \quad (\text{A.19})$$

is equivalent to the combined system of Eq. A.17 and Eq. A.18. We then define  $\{\mathbf{v}^{(n)}, n = 1, \dots, M'\}$ , with  $M' \leq N'$ , as a Gramm-Schmidt, orthonormal basis that spans the same

space as  $\{\beta^{(n)}\}$ . We define a  $9 \times 9$  dimensional projector matrix,  $\mathbf{P}$ , using

$$P_{ij} = \sum_{n=1}^{M'} v_i^{(n)} v_j^{(n)}. \quad (\text{A.20})$$

Let  $\{\mathbf{w}^{(k)}, k = 1, \dots, M\}$  be the complete set of  $M$  orthonormal eigenvectors of  $\mathbf{P}$  with zero eigenvalue. We then have

$$\mathbf{F}_k = \sum_{i=1}^9 w_i^{(k)} \mathbf{B}_i. \quad (\text{A.21})$$

In what follows, we consistently use the following symbols to denote the various different kinds of indices involved. All of the below indices are integers.

- $\mu$  : indexes the  $\mathbf{k}_\mu$ -point in the BZ.
- $a, b$  : are Cartesian vector indices.
- $j$  : refers to a set of symmetry-equivalent dynamical matrices in real space.
- $i$  : refers to a member in a set.
- $k$  : refers to the basis matrices of which the IFCs in real-space are a linear combination.
- $\sigma, \sigma'$  : refer to the atomic basis within a unit cell.
- $N_b(j)$  is the number of basis matrices in the  $j^{\text{th}}$  set.

The variables and quantities which we will be using are:

- $\mathbf{R}_{ji}$  : is the lattice vector corresponding to the  $j^{\text{th}}$  triplet set and  $i^{\text{th}}$  member.
- $\tau_{ji}, \tau'_{ji}$  : are the indices of the basis atoms of the  $j^{\text{th}}$  set and  $i^{\text{th}}$  member.
- $\mathbf{C}(j)$  : is a  $3 \times 3$  matrix for the  $1^{\text{st}}$  member of the  $j^{\text{th}}$  set. It is the  $\tau_{j1}, \tau'_{j1}$  block of the IFCs in real-space with separation vector  $\mathbf{R}_{j1}$ , i.e.,  $\mathbf{C}(j) = \mathbf{C}_{\tau_{j1}, \tau'_{j1}}(\mathbf{R}_{j1})$ .
- $\mathbf{F}_{jk}$  : for a given  $j$ ,  $\{\mathbf{F}_{jk}, k = 1, \dots, N_b(j)\}$  is a linearly independent set of  $N_b(j)$   $3 \times 3$  matrices (the basis matrices). They are related to  $\mathbf{C}(j)$  by

$$\mathbf{C}(j) = \sum_{k=1}^{N_b(j)} a_{jk} \mathbf{F}_{jk}, \quad (\text{A.22})$$



where the  $a_{jk}$  are to be determined by a fitting procedure to be described and are not determined by symmetry.

- $\mathbf{C}(\mu, \sigma, \sigma')$  : is a  $3 \times 3$  matrix giving the  $\sigma, \sigma'$  block in the IFCs at Bloch vector  $\mathbf{k}_\mu$ .
- $\mathbf{U}_{ji}$  : is the matrix transformation that relates an element in the set/member  $ji$  with an element with set/member  $ji$ , according to,  $\mathbf{C}_{\tau_{ji}\tau'_{ji}}(\mathbf{R}_{ji}) = \mathbf{U}_{ji}^T \mathbf{C}_{\tau_{j1}\tau'_{j1}}(\mathbf{R}_{j1}) \mathbf{U}_{ji}$ .

We consider the following quantity  $s$ , defined as,

$$s = \sum_{\sigma\sigma'} \sum_{ab\mu} \left| \sum_{\{i,j|\tau_{ji}=\sigma,\tau'_{ji}=\sigma'\}} [\mathbf{U}_{ji}^T \mathbf{C}(j) \mathbf{U}_{ji}]_{ab} e^{i\mathbf{k}_\mu \cdot \mathbf{R}_{ji}} - [\mathbf{C}(\mu, \sigma, \sigma')]_{ab} \right|^2 w(\mu), \quad (\text{A.23})$$

or

$$s(\{a_{jk}\}) = \sum_{\sigma\sigma'} \sum_{ab\mu} \left| \sum_{\{i,j,k|\tau_{ji}=\sigma,\tau'_{ji}=\sigma'\}} [\mathbf{U}_{ji}^T \mathbf{F}_{jk} \mathbf{U}_{ji}]_{ab} a_{jk} e^{i\mathbf{k}_\mu \cdot \mathbf{R}_{ji}} - [\mathbf{C}(\mu, \sigma, \sigma')]_{ab} \right|^2 w(\mu), \quad (\text{A.24})$$

where here we show the explicit dependence on the set of coefficients  $\{a_{jk}\}$  and the weights  $\{w(\mu)\}$ , which are arbitrary and can be chosen for a variety of convenient ends, such as phase-space weighting. The matrix,  $\mathbf{C}(\mu, \sigma, \sigma')$ , is determined by means described in preceding chapters of this thesis. The parameters  $\{a_{jk}\}$  are fitting parameters. Here we choose the triplet sets,  $(j, i)$ , for which we have

$$\| \mathbf{R}_{ji} + \tau'_{ji} - \tau_{ji} \| < r_c,$$

where  $r_c$  is some cutoff selected by the user.

To ensure that  $\tilde{\mathbf{C}}_{\tau\tau'}(\mathbf{k})$  is manifestly Hermitian, we divide the triplet sets into two groups. Within group (1) are those for which there exists a paired counterpart in a different set, i.e., a pair  $(j, i)$  and  $(j', i')$ , such that we have  $\mathbf{R}_{ji} = -\mathbf{R}_{j'i'}$  and  $\tau_{ji} = \tau'_{j'i'}$ ,  $\tau'_{ji} = \tau_{j'i'}$ . Within group (2) are those for which there exists no such pair. We let  $Q\{i, j|\tau_{ji} = \sigma, \tau'_{ji} = \sigma'\}$  denote the set corresponding to group (2) and  $P\{i, j|\tau_{ji} = \sigma, \tau'_{ji} = \sigma'\}$  denote the set corresponding to group (1) with only one of the pair members counted to

avoid overcounting. (Note that the triplet sets in group (1) occur in pairs.) This implies including half of the triplet sets in group (1) when performing the fit, and using the Hermiticity condition to deduce  $\mathbf{C}_{\tau\tau'}(\mathbf{R})$  if it belongs to an excluded triplet set. It should not matter which of a pair of triplet sets is included in the fit.

We then rewrite Eq. A.24 in terms of these two groups as:

$$\begin{aligned}
s(\{a_{jk}\}) &= \sum_{\sigma\sigma'} \sum_{ab\mu} \left| \sum_{Q\{i,j,k|\tau_{ji}=\sigma,\tau'_{ji}=\sigma'\}} a_{jk} [\mathbf{U}_{ji}^T \mathbf{F}_{jk} \mathbf{U}_{ji}]_{ab} e^{i\mathbf{k}\mu \cdot \mathbf{R}_{ji}} - [\mathbf{C}(\mu, \sigma, \sigma')]_{ab} \right|^2 w(\mu) \\
&+ \sum_{\sigma\sigma'} \sum_{ab\mu} \left| \sum_{P\{i,j,k|\tau_{ji}=\sigma,\tau'_{ji}=\sigma'\}} a_{jk} [\mathbf{U}_{ji}^T \mathbf{F}_{jk} \mathbf{U}_{ji}]_{ab} e^{i\mathbf{k}\mu \cdot \mathbf{R}_{ji}} - [\mathbf{C}(\mu, \sigma, \sigma')]_{ab} \right|^2 w(\mu) \\
&+ \sum_{\sigma\sigma'} \sum_{ab\mu} \left| \sum_{P\{i,j,k|\tau_{ji}=\sigma,\tau'_{ji}=\sigma'\}} a_{jk} [\mathbf{U}_{ji}^T \mathbf{F}_{jk} \mathbf{U}_{ji}]_{ba} e^{-i\mathbf{k}\mu \cdot \mathbf{R}_{ji}} - [\mathbf{C}(\mu, \sigma', \sigma)]_{ab} \right|^2 w(\mu).
\end{aligned}$$

We perform a constrained minimization on the quantity  $s(\{a_{jk}\})$  subject to the acoustic sum rule, which can be expressed by

$$\sum_{\mathbf{R}\tau'} [\mathbf{C}_{\tau\tau'}(\mathbf{R})]_{ab} = 0. \tag{A.25}$$

Here there is one equation for every combination of  $\tau$ ,  $a$ , and  $b$ , giving a total of  $9N$  constraint equations. The acoustic sum rule is therefore a further set of constraint equations linear in the fitting parameters. To determine these linear equations explicitly, we first define the quantity,

$$\begin{aligned}
A_{jk;\mu\sigma\sigma'ab} &= \sum_{Q\{i|\tau_{ji}=\sigma,\tau'_{ji}=\sigma'\}} [\mathbf{U}_{ji}^T \mathbf{F}_{jk} \mathbf{U}_{ji}]_{ab} e^{i\mathbf{k}\mu \cdot \mathbf{R}_{ji}} \\
&+ \sum_{P\{i|\tau_{ji}=\sigma,\tau'_{ji}=\sigma'\}} [\mathbf{U}_{ji}^T \mathbf{F}_{jk} \mathbf{U}_{ji}]_{ab} e^{i\mathbf{k}\mu \cdot \mathbf{R}_{ji}} + \sum_{P\{i|\tau_{ji}=\sigma',\tau'_{ji}=\sigma\}} [\mathbf{U}_{ji}^T \mathbf{F}_{jk} \mathbf{U}_{ji}]_{ba} e^{-i\mathbf{k}\mu \cdot \mathbf{R}_{ji}}.
\end{aligned} \tag{A.26}$$

The acoustic sum rule applies to the wave vector

$$\mathbf{k}_\mu = 0. \tag{A.27}$$

It is helpful to take the value of  $\mu$  from Eq. A.27, and define:

$$C_{jk;\sigma\sigma'ab} = A_{jk;\mu\sigma\sigma'ab}. \tag{A.28}$$

The acoustic sum rule is satisfied through the fitting parameters which satisfy the following system of linear equations:

$$\sum_{jk} a_{jk} C_{jk;\sigma\sigma'ab} = 0. \quad (\text{A.29})$$

This system of  $9N$  equations is not necessarily linearly independent. For example, in a system like diamond, there is only one linearly independent constraint equation in a set of 18 linear equations. To reduce Eq. A.29 to an equivalent smaller set of linearly independent equations, we use Gauss-Jordan elimination. Supposing that they reduce to a system of  $N_c$  linearly independent equations, we have

$$g^{(\nu)}(\{a_{jk}\}) \equiv \sum_{jk} a_{jk} c_{jk}^{(\nu)} = 0, \quad \nu = 1, \dots, N_c. \quad (\text{A.30})$$

By minimizing  $s(\{a_{jk}\})$  subject to the constraint relation in Eq. A.30, we have

$$\frac{\partial s(\{a_{jk}\})}{\partial a_{j'k'}^*} + \sum_{\nu=1}^{N_c} \lambda^{(\nu)} \frac{\partial [g^{(\nu)}(\{a_{jk}\})]^*}{\partial a_{j'k'}^*} = 0. \quad (\text{A.31})$$

Here  $\lambda^{(\nu)}$  are Lagrange multipliers, which need to be found. Eq. A.31 reduces to

$$\sum_{jk} M_{j'k',jk} a_{jk} + \sum_{\nu=1}^{N_c} \lambda^{(\nu)} c_{j'k'}^{(\nu)*} = b_{j'k'}, \quad (\text{A.32})$$

with

$$M_{j'k',jk} = \sum_{\mu\sigma\sigma'ab} w(\mu) A_{jk;\mu\sigma\sigma'ab} A_{j'k';\mu\sigma\sigma'ab}^* \quad (\text{A.33})$$

and

$$b_{jk} = \sum_{\mu\sigma\sigma'ab} w(\mu) A_{jk;\mu\sigma\sigma'ab}^* [\mathbf{C}(n, \sigma, \sigma')]_{ab}. \quad (\text{A.34})$$

If there are  $N_f$  fitting parameters (i.e., the  $a$ 's), then Eqs. A.30 and A.32 form a system of  $N_c + N_f$  equations with  $N_c + N_f$  unknowns.

## BIBLIOGRAPHY

- [1] W. Pauli, Verh. Deut. Phys. Ges. [3] **6**, 10 (1925).
- [2] M. Born and M. Blackman, Z. Physik **82**, 551 (1933); M. Blackman, Z. Physik **86**, 421 (1933).
- [3] R. B. Barnes, R. B. Brattain, and F. Seitz, Phys. Rev. **48**, 582 (1935).
- [4] M. Born and K. Huang, *Dynamical Theory of Crystal Lattices* (Oxford University Press, 1954).
- [5] L. Van Hove, N.M. Hugenholtz, and L.P. Howland, in *Quantum Theory of Many-Particle Systems* (W.A. Benjamin, New York, 1961); J. Kokkedee, Physica **28**, 374 (1962).
- [6] R.F. Wallis and A.A. Maradudin, Phys. Rev. **125**, 1277 (1962); V.S. Vinogradov, Sov. Phys.–Solid State **4**, 519 (1962); R.A. Cowley, Adv. Phys. **12**, 421 (1963).
- [7] R. Resta, Europhys. Lett. **22**, 133 (1993); R.D. King-Smith and D. Vanderbilt, Phys. Rev. B **47**, 1651 (1993).
- [8] A. Debernardi, S. Baroni and E. Molinari, Phys. Rev. Lett. **75**, 1819 (1995).
- [9] J. M. Meñendez and M. Cardona, Phys. Rev. B **29**, 2051 (1984).
- [10] P. Hohenberg and W. Kohn, Phys. Rev. **136**, B864 (1964).
- [11] W. Kohn and L. J. Sham, Phys. Rev. **140**, A1133 (1965).
- [12] J. P. Perdew and A. Zunger, Phys. Rev. B **23**, 5048 (1965); D. M. Ceperley and B. J. Alder, Phys. Rev. Lett. **45**, 566 (1980).
- [13] D. R. Hamann, M. Schlüter and C. Chiang, Phys. Rev. Lett. **43**, 1494 (1979).

- [14] D. Vanderbilt, Phys. Rev. B **32**, 8412 (1985).
- [15] L. Kleinman and D. M. Bylander, Phys. Rev. Lett. **48**, 1425 (1982).
- [16] E. L. Shirley, L. J. Terminello, J. E. Klepeis and F. J. Himpsel, Phys. Rev. B **53**, 10296 (1996).
- [17] R. P. Feynman, Phys. Rev. **56**, 340 (1939); H. Hellmann, *Einführung in die Quanten Theorie* (Deuticke, Leipzig, 1937), p. 285.
- [18] M. T. Yin and M. L. Cohen, Phys. Rev. B **26**, 3259 (1982).
- [19] J. Donahue, *The Structure of Elements* (Wiley, New York, 1974).
- [20] H.J. McSkimin and W.L. Bond, Phys. Rev. **105**, 116 (1957).
- [21] F. D. Murnaghan, *Proc. Nat. Acad. Sci.* **30**, 244 (1944).
- [22] J.L. Warren, J.L. Yarnell, G. Dolling, and R.A. Cowley, Phys. Rev. **158**, 805, 1967.
- [23] G. Dolling, *Inelastic Light Scattering in Solids* (IAEA, Vienna,1963), Vol II; G. Nilsson and G. Nelin, Phys. Rev. B **6**, 3777 (1972).
- [24] G. Nilsson and G. Nelin, Phys. Rev. B **3**, 364 (1971).
- [25] H.B. Huntington, in *Solid State Physics*, edited by F. Seitz and D. Turnbull (Academic, New York, 1958), Vol. 7.
- [26] Y.X. Zhao and I.L. Spain, Phys. Rev. B **40**, 993 (1989).
- [27] M.S. Dresselhaus and G. Dresselhaus, in *Light Scattering in Solids III*, edited by M. Cardona and G. Guntherodt, Topics in Applied Physics, Vol. 51 (Springer-Verlag, New York, 1982), Chap. 2, and references therein.

- [28] A.A. Maradudin, E.W. Montroll, G.H. Weiss, and I.P. Ipatova, in *Solid State Physics*, edited by H.E. Ehrenreich, F. Seitz, and D. Turnbull (Academic, New York, 1971), Suppl. 3, Chap. 6.
- [29] C. Kittel, *Introduction to Solid State Physics*, Sixth Edition (Wiley, New York, 1986).
- [30] X. Gonze and C. Lee, Phys. Rev. B **55**, 10355 (1997).
- [31] M. Balkanski, R.F. Wallis, and E. Haro, Phys. Rev. B **28**, 1928 (1983); J. M. Meñendez and M. Cardona, Phys. Rev. B **29**, 2051 (1984); T. R. Hart, R. L. Aggarwal, and B. Lax, Phys. Rev. B **1**, 638 (1970); P. A. Temple and C. E. Hathaway, Phys. Rev. B **7**, 3685 (1973); F. Cerdeira and M. Cardona, Phys. Rev. B **5**, 1440 (1972); R. K. Ray, R. L. Aggarwal, and B. Lax, in *Light Scattering in Solids*, edited by M. Balkanski (Flammarion, Paris, 1971), p. 288; R. S. Krishnan, Proc. Indian Acad. Sci. **24**, 45 (1946); E. Anastassakis, H. C. Hwang, and C. H. Perry, Phys. Rev. B **4**, 2493 (1971); W. J. Borer, S. S. Mitra, and K. V. Namjoshi, Solid State Commun. **9**, 1377 (1971).
- [32] A. Debernardi, S. Baroni, and E. Molinari, Phys. Rev. Lett. **75**, 1819 (1995); G. Lang, K. Karch, M. Schmitt, P. Pavone, A. P. Mayer, R. K. Wehner, and D. Strauch, Phys. Rev. B **59**, 6182 (1999).
- [33] M.E. Thomas, D. Blodgett, D. Hahn, and S. Kaplan, in SPIE Proceedings **5078**, Window and Domes Technologies VIII, 159 (2003).
- [34] A. Borghesi and G. Guizzetti, *Handbook of Optical Constants of Solids*, edited by E.D. Palik (Academic, London, 1998).
- [35] E.D. Palik, *Handbook of Optical Constants of Solids*, edited by E.D. Palik (Academic, London, 1998).
- [36] M.E. Thomas, R.I. Joseph, and W.J. Tropf, Appl. Opt. **27**, 239 (1988).

- [37] R.H. Stolen, Phys. Rev. B **11**, 767 (1975).
- [38] A. Debernardi, Solid State Commun. **113**, 1 (2000).
- [39] F. Widulle, T. Ruf, A. Göbel, E. Schönherr, and M. Cardona, Phys. Rev. Lett. **82**, 5281 (1999).
- [40] K.J. Yee, K.G. Lee, E. Oh, D.S. Kim, and Y.S. Lim, Phys. Rev. Lett. **88**, 105501 (2002).
- [41] M. Canonico, C. Poweleit, J. Menéndez, A. Debernardi, S.R. Johnson, and Y.H. Zhang, Phys. Rev. Lett. **88**, 215502 (2002).
- [42] M. Lax and E. Burstein, Phys Rev. **97**, 39 (1955).
- [43] G. Deinzer and D. Strauch, Phys. Rev. B **69**, 045205 (2004).
- [44] R. Kubo, J. Phys. Soc. Japan **12**, 570 (1957); S. Doniach and E. H. Sondheimer, *Green's Functions for Solid State Physicists* (Benjamin, London, 1974).
- [45] R.A. Cowley, Proc. Phys. Soc. **84**, 281 (1964).
- [46] A.A. Maradudin and A.E. Fein, Phys Rev. **128**, 2589 (1962).
- [47] A. Debernardi, M. Alouani, and H. Dreyse, Phys. Rev. B **63**, 064305 (2001).
- [48] G. Deinzer, G. Birner, and D. Strauch, Phys. Rev. B **67**, 144304 (2003).
- [49] L. Van Hove, N.M. Hugenholtz and L.P. Howland, in *Quantum Theory of Many-Particle Systems* (W.A. Benjamin, New York, 1961).
- [50] G. Dolling and R.A. Cowley, Proc. Phys. Soc. **88**, 463 (1966).
- [51] G. Placzek, B.R.A. Nijboer, and L. Van Hove, Phys. Rev. **82**, 392 (1951).
- [52] M. Born, Rep. Prog. Phys. **9**, 294 (1943).

- [53] M. Ferconi and M.P. Tosi, *J. Phys: Condes. Matt.* **3**, 9943 (1991).
- [54] D. Pines, *Elementary Excitations in Solids* (W.A. Benjamin, New York, 1963).
- [55] K. Lonsdale, *Proc. Roy. Soc. A* **179**, 8 (1942).
- [56] V.Y. Naysh, *Fiz. Metal.* **77**, 48 (1994).
- [57] P. Rabe, G. Tokiehn, and A. Werner, *J. Phys. C* **12**, L545 (1979).
- [58] A. Kirfel, J. Grybos, and V.E. Dmitrienko, *Phys. Rev. B* **66**, 165202 (2002).
- [59] O.H. Nielsen and W. Weber, *J. Phys. C* **13**, 2449 (1980).
- [60] G. Lang, K. Karch, M. Schmitt, P. Pavone, A.P. Mayer, R.K. Wehner and D. Strauch, *Phys. Rev. B* **59**, 6182 (1999).
- [61] F. Occelli, M. Krisch, F. Sette, R. Le Toullec, C. Masciovecchio, and J.P. Rueff, *J. Chem. Phys.* **117**, 5859 (2002).
- [62] H. Shimizu, H. Tashiro, T. Kume, and S. Sasaki, *Phys. Rev. Lett.* **86**, 4568 (2001).
- [63] M. Grimsditch, P. Loubeyre, and A. Polian, *Phys. Rev. B* **33**, 7192 (1986)
- [64] Y. Fujii, N.A. Lurie, R. Pynn, and G. Shirane, *Phys. Rev. B* **10**, 3647 (1974).
- [65] T. Iitaka and T. Ebisuzaki, *Phys. Rev. B* **65**, 012103 (2001).
- [66] T. Nakamura and H. Nagara, *High Pressure Res.* **23**, 3 (2003).
- [67] J. Tse, D. Klug, V. Shpakov, and J. Rodgers, *Solid State Comm.* **122**, 557 (2002).
- [68] T. Tsuchiya and K. Kawamura, *J. Chem. Phys.* **117**, 5859 (2002).
- [69] K. Rościszewski, B. Paulus, P. Fulde, and H. Stoll, *Phys. Rev. B* **62**, 5482 (2000).
- [70] M. Dion, H. Rydberg, E. Schröder, D.C. Langreth and B.I. Lundqvist, *Phys. Rev. Lett.* **92**, 246401 (2004).



[71] C. Kittel, *Introduction to Solid State Physics*, Third Edition (Wiley, New York, 1966).